Adaptation to ER-stress via serine glycine metabolism licences STING signalling and CMV control in intestinal epithelial cells

Authors

Felix Wottawa[1*], Björn Becker[2*], Mohamed Bakr[1*], Lisa Mayr[3], Julia Kugler[1], Samuel J Windross[4], Laura Neises[2], Silke van den Bossche[1], Nassim Kakavand[1], Florian Tran[1,13], Lina Welz[1,13], Julian Schwärzler[3], Zoltán Bánki[5] Stephanie Stengel[1], Go Ito[6], Olivia Coleman[7], Christian Jaeger[8], Eric Koncina[9], Elisabeth Letellier[9], Dirk Haller[7], Søren R Paludan[4], Richard Blumberg[10], Arthur Kaser[11], Luka Cicin-Sain[12], Stefan Schreiber[1,13], Timon Adolph[3], Philip Rosenstiel[1+] , Johannes Meiser[2+] and Konrad Aden[1,13+]

Affiliation

1 Institute of Clinical Molecular Biology, Christian-Albrechts-University and University Hospital Schleswig-Holstein, Campus Kiel, 24105 Kiel, Germany

2 Luxembourg Institute of Health, Department of Cancer Research, Luxembourg

3 Department of Internal Medicine I, Gastroenterology, Hepatology, Metabolism & Endocrinology, Medical University of Innsbruck, Innsbruck, Austria

4 Department of Biomedicine, Aarhus University, Aarhus, Denmark

5 Institute of Virology, Department of Hygiene, Microbiology and Public Health, Medical University of Innsbruck, Innsbruck, Austria.

6 Department of Gastroenterology and Hepatology, Tokyo Medical and Dental University, Tokyo, Japan;

7 Chair of Nutrition and Immunology, TUM School of Life Sciences, Technical University of Munich

23 8 Luxembourg Centre for Systems Biomedicine, University of Luxembourg, Esch-sur-Alzette,
24 Luxembourg
25 9 Faculty of Science, Technology and Medicine, Department of Life Sciences and Medicine,
26 Université du Luxembourg
27 10 Gastroenterology Division, Department of Medicine, Brigham and Women's Hospital,
28 Harvard Medical School, Boston, MA.
29 12 Division of Gastroenterology and Hepatology, Department of Medicine, Addenbrooke's
30 Hospital, University of Cambridge, Cambridge, England, UK
31 12 Helmholtz Zentrum für Infektionsforschung, Braunschweig, Germany
32 13 Department of Internal Medicine I., Christian-Albrechts-University and University Hospital
33 Schleswig-Holstein, Campus Kiel, 24105 Kiel, Germany
34
35 *These authors contributed equally
36 [+] shared senior authorship

37 **Correspondence to:**
38 Konrad Aden, MD
39 Department of Internal Medicine I,
40 University Medical Center Schleswig Holstein
41 Rosalind Franklin Straße 11,
42 24105 Kiel, Germany
43 T: +49-431 500-22455,
44 F: +49 431-500-15168,
45 E-Mail: k.aden@ikmb.uni-kiel.de
46

Philip Rosenstiel, MD
Professor of Molecular Medicine
Director, Institute of Clinical Molecular Biology,
Christian-Albrechts-University Kiel
Rosalind Franklin Straße 11, 24105 Kiel, Germany
T: +49-431 500-15111,
F: +49 431-500-15168,
E-Mail: p.rosenstiel@mucosa.de

Johannes Meiser, PhD
Group Leader of Cancer Metabolism Group
Department of Cancer Research
Luxembourg Institute of Health
84, Val Fleuri,
L-1526 Luxembourg
Luxembourg
T: +352 26970-453
Email: Johannes.Meiser@lih.lu

Disclosures: The authors have no conflict of interest.

Author Contributions

PR, KA, JM, FW and BB designed the study.

FW, BB, MB, LM, JK, SJW, LN, SB, NK, FT, LW, SSt, GI, OC, CJ, EK, EL, DH, SRP, TA, JM, PR and KA performed experiments and analyzed data.

LCS, RB, AK and SSc provided intellectual input and guidance.

PR, KA, JM, FW and BB planned the project and supervised the experiment.

PR, KA, JM and FW wrote the manuscript.

Highlights:

- **Chronic ER stress abrogates gut epithelial cGAS/STING signalling and increases susceptibility to CMV infection**
- **Chronic ER stress increases serin-glycin metabolism to counterbalance reactive oxygen species overload in IECs**
- **Abrogation of serine-glycine metabolism exacerbates ROS generation and inhibits epithelial STING signalling.**
- **Pharmacologic ROS scavenging in ER stressed epithelium restores cGAS/STING activation and leads to improved control of CMV infection**

Abstract:

Mucosal cytomegalovirus (CMV) infection represents a leading cause for complicated disease behaviour and proctocolectomy in patients with inflammatory bowel disease (IBD). Using a genetic loss-of-function mouse model of the hypomorphic IBD risk gene X-box-binding protein 1 (*XBP1*), isotope-assisted metabolomics and pharmacologic approaches, we unravel the molecular control of gut epithelial STING signalling by unresolved endoplasmic reticulum (ER) stress. We demonstrate that unresolved epithelial ER stress, evoked by *Xbp1* deficiency, leads to exhausted STING signalling and an impaired ability to control CMV infection, which is driven by the generation of reactive oxygen species (ROS). ROS generation is controlled by cellular glycine influx and de-novo serin synthesis enabling glutathione production, which can be pharmacologically exploited to restrore STING signaling. Pharmacological scavenging of ROS with N-acetly cysteine restores epithelial STING signalling and limits CMV infection in

96 IECs. Our findings unravel the serine-glycine dependent metabolic control by ER stress that
97 licences STING signaling and susceptibility to infection in gut epithelium.
98 **[Words: 156/160]**

99 **Important abbreviations used in this paper:**

100 *2'3'-cGAMP*: 2'3' linked cyclic guanosine monophosphate-adenosine monophosphate; *ATF6*:
101 Activating transcription factor 6; *BI*: BI-4924; *cGAS*: Cyclic GMP-AMP synthase; *CMV*:
102 cytomegalovirus; *CORE*: consumption and release; *CXCL10*: C-X-C Motif Chemokine Ligand
103 10; *DAMP*: danger-associated molecular pattern; *DMXAA*: dymethylxanthone acetic acid;
104 *dsDNA*: double-stranded DNA; *ER*: endoplasmic reticulum; *ER-stress*: endoplasmic reticulum
105 stress; *GGC*: dipeptide γ-glutamyl cysteine; *GPX*: glutathione peroxidases; *GS*: gluthathione
106 synthetase; *GSH*: gluthathione; *GSSG*: glutathione disulphide; *IBD*: inflammatory bowel
107 disease; *IECs*: intestinal epithelial cells; *IFNβ*: interferon beta; *IL*: interleukin; *IRF3*:
108 interferon-regulatory-factor 3; *ISG*: interferon-stimulated gene; *L. monocytogenes*: *Listeria*
109 *monocytogenes*; *LPO*: lipid peroxidation; *MCMV*: murine cytomegalovirus; *MEF*: mouse
110 embryonic fibroblasts; *MOI*: multiplicity of infection; *NAC*: N-acetly cysteine; *PAMP*:
111 pathogen-associated molecular pattern; *ROS*: reactive oxygen species; *RSL3*: RAS-selective
112 lethal 3; *S/G*: serine-glycine; *SNP*: single nucleotide polymorphism; *SSP*: serine *de novo*
113 synthesis pathway; *STING*: stimulator of interferon genes; *TBK1*: tank-binding kinase 1; *TM*:
114 Tunicamycin; *TNF*: tumor necrosis factor; *UC*: ulcerative colitis; *UPR*: unfolded protein
115 response; *XBP1*: X-box binding protein 1

116 **Introduction:**

117 Inflammatory bowel disease is a chronic relapsing inflammatory disorder of the gastrointestinal
118 tract. Although the introduction of targeted inhibition of pro-inflammatory pathways (e.g. anti-
119 TNF, anti-IL12/23) has significantly improved patient care, disease-associated complications
120 such as IBD-related hospitalizations and surgery still contribute to the major socioeconomic
121 burden of IBD (1). IBD-related cytomegalovirus (CMV) infections have seen a steep rise in
122 the past years and recurrent CMV-infections in IBD patients are associated with increased risk
123 of hospitalization and proctocolectomy (2). Although meta-analysis of retrospective clinical

124 studies indicate that disease extent and disease severity directly correlate with CMV colitis
125 risk, the underlying molecular mechanisms that drive susceptibility to CMV infection in IBD
126 remain enigmatic (3).
127 Endoplasmic reticulum stress (ER-stress) describes a state of disrupted cellular homeostasis,
128 which occurs if the balance between ER folding capacity and protein load is disturbed(4–9).
129 Cells with a high secretory demand such as intestinal epithelial cells (IECs, more specifically
130 Paneth and Goblet cells) are especially prone to accumulate unfolded proteins and thus highly
131 susceptible to ER-stress-associated pathologies (9,10). Ultimately, ER-stress triggers a
132 detrimental inflammatory reaction that drives mucosal tissue damage in human IBD (11,12).
133 The unfolded protein response (UPR) consists of three major pathways (specifically, the
134 IRE1/XBP1-, PERK/ATF4- and ATF6-pathway) and aims to reinforce ER homeostasis, thus
135 counteracting inflammation. Specific single-nucleotide-polymorphisms (SNPs) in the *X-box*
136 *binding protein 1* (*XBP1*) gene result in hypomorphic variant predisposing for ER-stress and
137 have been identified to mediate increased IBD susceptibility and mechanistically augment
138 epithelial-derived mucosal inflammation (13,14).
139 The cGAS/STING (cyclic GMP-AMP synthase/stimulator of interferon genes) pathway allows
140 nucleic acid sensing and pathogen defence, by directly sensing cytosolic double-stranded DNA
141 (dsDNA) derived from viruses (e.g., CMV) or cyclic dinucleotides derived from intracellular
142 bacteria (e.g., *Listeria monocytogenes*) (15–17). After binding of cytosolic dsDNA and
143 subsequent 2′3′-cGAMP (2’3’ linked cyclic guanosine monophosphate-adenosine
144 monophosphate) production by cGAS, STING is activated. STING is an ER-resident adaptor
145 protein which mediates activation of TBK1 (Tank-binding-kinase 1) and IRF3 (Interferon-
146 regulatory-factor 3), controlling interferon beta (IFNβ) production and secretion. IFNβ belongs
147 to the family of type I IFNs and induces a variety of antiviral, immunomodulatory or
148 antiproliferative interferon-stimulated genes (ISGs), e.g. *CXCL10* (17). As such, cGAS/STING

149 signaling is critically involved in type I IFN induction during CMV infection, and CMV
150 actively antagonizes STING-mediated IFN induction, underscoring the potential role of
151 STING as a crucial first line of defense against CMV infection (18–20). Due to its localization
152 as an ER-resident protein, it is postulated that STING function is closely intertwined with ER
153 homeostasis. To which extent disturbance of the UPR directly affects cGAS/STING sensing
154 is not known. Several studies support the notion that acute ER stress is an important upstream
155 modulator of STING activation in response to PAMPs and DAMPs (21,22) and pro-
156 regenerative IL-22 signaling (23). We hypothesised that chronic unresolved ER stress directs
157 epithelial STING signaling in response to CMV infection. We find that chronic ER stress
158 instigates immune exhaustion of the STING pathway in the intestinal epithelium which renders
159 IECs susceptible to CMV infection. Using a genetic model of chronic ER stress, i.e. conditional
160 deletion of *Xbp1* in intestinal epithelial cells (*Xbp1*$^{\Delta IEC}$), we show that immune exhaustion of
161 STING depends on accumulation of reactive oxygen species due to insufficient scavenging by
162 glutathione. We show that epithelial STING signaling relies on the metabolic control of serine-
163 glycine dependent glutathione synthesis during ER stress, which allows to cope with
164 environmental challenges, such as CMV infection.

165 **<u>Results & Discussion:</u>**

166 **Chronic ER-stress suppresses STING signaling in intestinal epithelial cells**

167 Chronic intestinal inflammation has been associated with risk for CMV infection in IBD. As
168 cGAS/STING signaling is involved in CMV control and cytomegalovirus induces the unfolded
169 the *Xbp1* branch of the unfolded protein response(24), we tested a potential crosstalk between
170 chronic ER stress and cGAS/STING signaling in response to CMV infection.

171 We used a transgenic mouse model that allows intestinal epithelial deletion of the *Xbp1* gene
172 in mice (*Xbp1*$^{\Delta IEC}$, *Xbp1*$^{fl/fl}$) or and knockdown in a non-transformed small intestinal epithelial

173 cell line by CRISPR Cas9 gene editing (Mode-K cells; *iCtrl* and *iXbp1*) (5,6). We first observed
174 that chronic epithelial ER stress impairs STING expression in *Xbp1*$^{\Delta IEC}$ mice when compared
175 to *Xbp1*$^{fl/fl}$ (WT) littermates, which was unrelated to STING transcription (Fig. 1 A, B, Fig.
176 S1A, B). In line with this, we observed reduced expression of *Cxcl10* and *Ifnb* in small
177 intestinal crypts from *Xbp1*$^{\Delta IEC}$ mice, indicative of reduced STING/IFN-I activity (Fig. 1C, Fig.
178 S1C). Next, we investigated whether chronic ER stress impairs cGAS/STING signalling. To
179 do so, we stimulated *iCtrl* and *iXbp1* IECs with double-stranded DNA (dsDNA) and observed
180 a nearly complete abrogation of STING activity (Fig. S1D) and *Cxcl10* expression (Fig. S1E)
181 in *Xbp1*-deficient IECs. This observation was phenocopied by chemical induction of chronic
182 ER stress with low-dose Tunicamycin 24h prior to dsDNA exposure (Fig. S1F, G). In contrast,
183 induction of acute ER stress potently activated the cGAS/STING pathway (Fig. S1H, I). These
184 findings suggested that unresolved ER stress promoted exhaustion of the STING pathway with
185 impaired type I IFN production in response to pathogen sensing. Indeed, the STING agonist
186 DMXAA activated STING and TBK1 phosphorylation in iCtrl but to a lesser extent in iXbp1
187 IECs (Fig. 1D), which was accompanied by impaired *Cxcl10* and *Ifnb* induction (Fig. 1E, F).
188 Moreover, we validated the impact of chronic ER stress on epithelial STING signalling using
189 an independent transgenic mouse model, i.e. *nAtf6*^{IEC} VilCreERT2 mice carrying a Tamoxifen-
190 inducible intestinal epithelial *Atf6* overexpression (leading to constitutive ER stress(25,26)).
191 Tamoxifen-induced overexpression of *Atf6* led to epithelial STING suppression (Fig. S1J, K).
192 Collectively, our data demonstrated that chronic ER stress suppresses STING signalling in the
193 intestinal epithelium.

194 **ER stress mediated STING exhaustion increases susceptibility to CMV infection in IEC`s**

195 To test if ER stress-induced perturbation of the STING signalling links to susceptibility towards
196 infection, we infected chronically stressed i*Xbp1* Mode-K IECs (and controls) with murine
197 CMV (MCMV). We stimulated iCtrl and i*Xbp1* cells with xy copies of MCMV for xy h and

198 assessed STING-dependent type I IFN production. Indeed, iCtrl IECs responded to MCMV
199 infection with STING activation, type I IFN induction and subsequent viral containment when
200 compared to i*Xbp1* IECs, which failed to induce type I IFNs (Fig. 1G, Fig. S1L) and showed
201 increased CMV loads (Fig. 1H). To verify the impact of epithelial STING signalling on CMV
202 infection *in vivo*, we challenged *Xbp1*$^{fl/fl}$ and *Xbp1*$^{\Delta IEC}$ mice with MCMV intraperitoneally and
203 assessed the degree of intestinal inflammation five days after the initial infection, as described
204 previously (27,28). In line with previous reports, the total viral load within the intestinal
205 mucosa was not detectable at day of sacrifice. However, we observed increased severity of
206 enteritis by a semiquantitative histology score in *Xbp1*$^{\Delta IEC}$, but not in *Xbp1*$^{fl/fl}$ mice (Fig. 1I, J)
207 5 days after CMV exposure. This observation confirmed that MCMV infection controlled the
208 inflammatory tone in genetically susceptible mice that exhibit chronic epithelial ER stress. To
209 test whether the observed STING exhaustion is relevant to other pathogen infections, we
210 further infected IECs with the intracellular pathogen *Listeria monocytogenes*. As described
211 before (29), *L. monocytogenes* infection resulted in strong type I IFN induction in the iCtrl
212 cells, which was barely detectable in i*Xbp1* IECs (Fig. S1M, N) . These data indicate that
213 chronic ER stress results in a functional impairment of STING signalling which leads to
214 inefficient pathogen clearance in the intestinal epithelium.

215 **ER stress induces ROS-dependent metabolic adaptation to maintain STING signalling**

216 We next aimed at identifying the underlying molecular processes that links chronic ER stress
217 with impaired STING signalling in IECs. Chronic ER stress has been associated with
218 fundamental changes of amino acid metabolism in the context of carcinogenesis (30). We
219 therefore tested the hypothesis that ER stress mediated alterations in amino acid metabolism
220 drives STING exhaustion under conditions of chronic ER stress. We performed an unbiased
221 metabolic profiling by assessing consumption and release (CORE) rates from the cell culture

222 medium, steady-state levels of intracellular metabolites and relative flux distribution through
223 central carbon metabolism using stable isotope-assisted metabolomics (Fig. S2A). Intracellular
224 analysis of metabolite steady-state levels showed significant increases of various metabolites.
225 Most consistently, we observed a strong increase of intracellular metabolites in i*Xbp1*, that are
226 required for glutathione synthesis, such as glycine, glutamate and cystine (Fig. 2A).
227 Glutathione (GSH) is the most abundant intracellular antioxidant, and GSH synthesis is a two-
228 step process in which the glutamate-cysteine ligase catalyzes the rate limiting step to form the
229 dipeptide γ-glutamyl cysteine (GGC) from cysteine and glutamate (31,32). Intracellular
230 cysteine availability can be increased via the cystine/glutamate antiporter *Slc7a11* and is
231 enhanced in response to ROS formation (Fig. 2B) (33). To test whether an atltered metabolic
232 state towards increased GSH synthesis is seen upon chronic ER stress we assessed CORE rates
233 in iCtrl and i*Xbp1* cells and observed increased glutamine consumption and a striking switch
234 from glutamate consumption towards glutamate release (Fig. 2C), pointing toward increased
235 cystine/glutamate exchange in i*Xbp1* cells. We further validated the observation of increased
236 glutamate release rates upon chronic ER stress in intestinal organoids stimulated with
237 Tunicamycin (Fig. S2F). Although ER stress induced a strong ROS signature based on the
238 amino acid exchange rates, central carbon metabolism remained largely unchanged in i*Xbp1*
239 cells. Following a metabolic flux analysis with [U-^{13}C]glucose and [U-^{13}C]glutamine no
240 striking differences have been observed, suggesting that cells primarily repond to ROS stress
241 by alterted amino acid exchange rates. (FigS2 B-E).
242 Based on this observation we tested the hypothesis that ER-stress induces a metabolic shift
243 towards increased intracellular availability of amino acids needed for GSH synthesis. Hence,
244 we repeated the metabolic profiling in response to the chemical ER stress inducer Tunicamycin
245 (TM). Indeed, TM treatment induced a similar, dose-dependent glutamate release in both iCtrl
246 and i*Xbp*1 cells (Fig. 2D). Cystine uptake rates increased upon TM treatment along with a

247 switch from glycine release towards glycine uptake (Fig. 2E, F). Most likely, the glycine switch
248 can be explained by an increased glycine demand for GSH synthesis. Generally, cells satisfy
249 their glycine demand from serine catabolism and show net excretion of glycine. However, in
250 context of ER stress the serine derived glycine does not seem to be sufficient for IECs which
251 causes a glycine switch from net excretion to net consumption (Fig. S2G). To further test the
252 hypothesis that unresolved ER stress induces a metabolic switch aiming to mount sufficient
253 GSH levels, we also observed increased expression of the glutamate/cystine antiporter *Slc7a11*
254 and increased intracellular GSH levels in response to ER stress (Fig. 2G). The primordial
255 function of GSH is to counterbalance free radicals derived from ROS by being oxidized to
256 glutathione disulphide (GSSG) (34,35) (Fig. S2H). We therefore assessed GSH, GSSG levels
257 and the ratio of GSH/GSSG. Despite increased steady state levels of GSH, GSSG and the ratio
258 of GSH over GSSG was reduced in *iXbp*1 cells compared to *iCtrl* cells suggesting an
259 unbalanced intracellular ROS homeostasis (Fig. 2H-J).
260 The neutralization of reactive oxygen species is conducted via the reduction of hydroperoxides
261 via oxidation of reduced GSH into its disulfide form GSSG by glutathione peroxidases (GPX).
262 We therefore tested the expression of glutathione peroxidase (GPX) 1-4 expression and
263 observed that i*Xbp1* cells showed a significant reduction of GPX 1-4, indicating that reduced
264 GPX expression accounts for decreased GSH/GSSG ratio in i*Xbp1* cells that ultimately would
265 result in increased accumulation of ROS in chronic ER-stressed cells (Fig. S2I). We therefore
266 assessed whether ER-stress results in increased ROS generation in IECs, as postulated
267 previously for e.g. mouse embryonic fibroblasts (MEF) (36). Indeed, we noted increased ROS
268 levels at baseline in i*Xbp1* cells compared to i*Ctrl* cells which was further augmented in
269 response to TM treatment (Fig. 2J). As GSH is also utilized to counterbalance ROS-dependent
270 lipid peroxidation (LPO) (34,35,37,38), we further assessed LPO levels, which were also
271 significantly increased in i*Xbp1* cells and further increased upon acute TM treatment (Fig. 2K).

272 Altogether, our metabolic profiling revealed that i) ER-stress induces a metabolic shift towards
273 increased GSH synthesis to counterbalance ROS and that ii) chronic ER stress renders cells
274 into a state of ROS accumulation. Based on our data we hypothesize that this metabolic
275 adaptation process represents a bottleneck for IECs to maintain healthy ROS homeostasis while
276 excessive ROS levels might impair proper STING signalling in response to CMV infection.

277 **Serine and glutathione metabolism is a critical gatekeeper of STING function in intestinal**
278 **epithelial cells**

279 Serine has multiple important roles to support cellular functionality (39,40). Besides protein
280 biosynthesis, serine represents a building block for sphingolipid synthesis and its catabolism
281 provides essential building blocks for nucleotides synthesis. Consequently, serine/glycine
282 (S/G) starvation has gained much attention as a dietary anticancer intervention (41). Alternative
283 to anabolic needs, catabolism of serine via the mitochondrial folate pathway can also give rise
284 to net production of ATP (42). Additionally, serine catabolism also generates glycine which
285 represents an essential building block for GSH synthesis. Finally, serine derived one-carbon
286 units can be oxidized via the one-carbon cycle to generate NADPH, an important co-factor for
287 the reduction of oxidised glutathione. Hence, we predicted that upon ER-stress and
288 concomitant elevated ROS levels, serine metabolism becomes polarized to counterbalance
289 ROS levels by providing glycine and NADPH. To validate the hypothesis that serine and
290 glutathione metabolism is a critical gatekeeper in response to ER-stress aiming to maintain
291 STING function, we used the following approach: we exposed iCtrl/i*Xbp1* to serine-glycine
292 free (S/G^-) cell culture medium to deprive GSH precursors. A decrease of intracellular glycine
293 and serine levels as well as an increase in GGC confirmed functional consequences of S/G
294 starvation. (Fig. S3A-C). In context of S/G deprivation the cell is able to induce a metabolic

295 compensatory mechanism of the serine *de novo* synthesis pathway, aiming to generate serine
296 from glucose via phosphoglyceratedehydrogenase (*Phgdh)* (Fig. 3A).
297 We therefore applied [U-^{13}C]-glucose tracing to monitor the relative glucose flux through the
298 serine *de novo* synthesis pathway (SSP) which can act as a compensatory mechanism upon
299 serine starvation. Illustrated by the M+3 serine isotopologue, serine starvation strongly
300 increased SSP (Fig. S3D) upon S/G starvation. Notably, this increased SSP activity was not
301 sufficient to fully compensate S/G deprivation with regard to serine, glycine or GGC levels
302 (Fig. S3A-C). Of note, at standard conditions, the SSP activity of i*Xbp1* cells was not increased
303 compared to iCtrl cells (Fig. S3D).
304 We next tested the direct impact of S/G starvation on ROS and LPO formation in iCtrl and
305 i*Xbp1* cells. As S/G starvation led to a compensatory activation of the SSP, which might
306 directly feed into GSH synthesis we combined S/G starvation with the inhibition of PHGDH,
307 the rate limiting enzyme of the SSP pathway, by using the specific and competitive inhibitor
308 BI-4916 (BI, Fig. 3A) (43,44). As expected, BI treatment blocked SSP and dual perturbation
309 with BI and S/G starvation further reduced intracellular serine and GSH levels, confirming the
310 efficacy of our treatment (Fig. 3B, C, Fig. S3E). Interestingly, GSH depletion was more
311 pronounced in i*Xbp1* cells compared to iCtrl cells (Fig. 3C).
312 In order to assess whether the metabolic shift towards GSH synthesis functionally led to
313 increased accumulation of ROS levels and LPO, we assessed ROS and LPO levels in i*Xbp1*
314 and iCtrl cells. We found that the deprivation of S/G w/wo the inhibition of serine *de novo*
315 synthesis led to increased accumulation of LPO and ROS, which was again increased in i*Xbp1*
316 cells (Fig. 3D, E).
317 Finally, to formally show that deprivation of the compensatory serine metabolism disrupts
318 epithelial STING signalling, we performed a single (S/G deprivation) or dual (S/G deprivation
319 + *de novo* synthesis inhibition) perturbation of serine metabolism of iCtrl cells and stimulated

320 with the STING agonist DMXAA. While S/G starvation alone had no significant impact on
321 *Cxcl10* expression of DMXAA treated iCtrl cells, dual perturbation (S/G + BI) resulted in a
322 strong and significant reduction of *Cxcl10* expression. (Fig. 3F) and decreased phosphorylation
323 of STING and TBK (Fig. 3G). Altogether our data show that serine-glycine metabolism serves
324 as a critical gatekeeper to facilitate STING/IFN-I signalling in the stressed intestinal epithelial
325 cells.

326 **Serine-glycine metabolism is increased in the intestinal epithelium of IBD patients**

327 To validate whether serine-glycine metabolism also provides a functional metabolic adaptation
328 process to facilitate IFN-I signalling in the inflamed mucosa of IBD patients, we used available
329 transcriptome datasets from UC patients. Doing so we observed that the expression of genes
330 involved in compensatory serine-glycine metabolism (*PHGDH, SLC7A11, ALDH1L2,*
331 *MTHFD1L, MTHFD2, SHMT2*) significantly increased with endoscopic and histologic
332 inflammation (Fig. S4A, B). Notably the induction of genes involved in the serine-glycine
333 metabolism also significantly correlated with the induction of interferon-inducible genes (ISG
334 score), indicating that indeed serine-glycine metabolism is essential in licensing mucosal IFN-
335 I production (Fig. S4C, D).

336 To further show that induction of serine-glycine metabolism corresponds with disease activity
337 in IBD we assessed the induction of genes involved in serine-glycine metabolism in clinical
338 responder and non-responder IBD patients and observed that targeted treatment with biologic
339 therapies leads to significant downregulation of serine-glycine metabolism in therapy
340 responders (Fig. S4E). We further assessed single-cell RNA sequencing data obtained from the
341 SCP259 scRNA-Seq IBD dataset (colon mucosa of 18 UC patients and 12 healthy individuals
342 (45)) to understand whether the observed association of serine metabolism and IFN-I induction
343 is specifically present in IECs. We confirmed that genes involved in ER-stress, serine

344 metabolism and ISG production are expressed in intestinal epithelial cells and clusters with
345 high serine score were attributed to secretory cell types, such as Paneth cells and goblet cells
346 (Supplementary Figure F,G).

347 **Restoration of glutathione function restores STING signalling and CMV control in**
348 **intestinal epithelial cells**

349 Having shown that serine metabolism orchestrates STING signalling in IECs and that this
350 metabolic process is also present in IECs of IBD patients, we tested the hypothesis that
351 pharmacological ROS inhibition restores epithelial STING signalling and thereby reinforces
352 CMV protection. We therefore treated iCtrl and i*Xbp1* cells with the antioxidant N-acetyl
353 cysteine (NAC). NAC treatment successfully reverted the observed glutamate switch in i*Xbp1*
354 cells (Fig. 4A) and lowered intracellular ROS and LPO levels (Fig. 4B, C). In addition, NAC-
355 treatment completely restored DMXAA-induced pSTING and pTBK1 levels in i*Xbp1* cells
356 (Fig. 4D), indicating that indeed ER-stress impairs STING signalling via ROS generation. As
357 we had shown that *Xbp1*-deficient cells show decreased GPX4 expression and increased ROS
358 formation, we further confirmed that GPX4 inhibition, using the GPX4 inhibitor RSL3, led to
359 a nearly complete abrogation of STING signalling, which was completely rescued in the
360 presence of NAC (Fig. 4E-G). Along the same line the impact of combined S/G starvation and
361 PHGDH inhibition on STING signalling was fully reverted in the presence of NAC (Fig. 4H,
362 I). Finally, we wondered whether restoration of STING signalling via NAC directly improves
363 CMV control in IECs. To this purpose we co-treated MCMV infected iCtrl and i*Xbp1* cells
364 with NAC. In line with our hypothesis i*Xbp1* cells showed a robust restoration of type I IFN
365 signalling (Fig. 4J, K) which further resulted in reconstituted suppression of MCMV viral load
366 (Fig. 4L).
367

368 **Discussion:**

369 Mucosal CMV infection is a leading cause of complicated disease behaviour in IBD. However,
370 the underlying molecular pathophysiology driving increased susceptibility towards CMV
371 colitis in IBD patients is poorly understood. Our data provide a novel molecular nexus on how
372 chronic ER-stress paves the susceptibility to CMV infection and thereby generate a molecular
373 inside into a well-established and highly relevant disease complication in IBD. We show that
374 i) chronic ER-stress generates a molecular susceptibility to CMV infection via impairment of
375 STING signalling. We further provide evidence that ii) the functional impairment of epithelial
376 STING signalling depends on intracellular ROS generation. In addition, we show that iii) ER-
377 stressed IECs aim to counterbalance ROS and reinstall STING signalling by funnelling the
378 cellular metabolic flux towards serine-glycine dependent glutathione synthesis. Our data
379 indicate that serine-glycine metabolism is essential in counterbalancing ER-stress induced ROS
380 and licences STING signalling in the intestinal epithelium. We postulate that this mechanism
381 has a profound impact on host immunity and might provide a layer of susceptibility towards
382 pathogen infection in the inflamed mucosa of IBD patients.

383 In this context it needs to be noted that recent data indicate that the intestinal epithelium indeed
384 presents the primary sensor of mucosal CMV infection, as IECs have been shown to be
385 permissive to CMV replication and elicit a proinflammatory mucosal immune signal in
386 response to CMV signalling (46). Over thirty years ago is has been described that HCMV
387 infection increases the glycolytic flux of host cell and that glycolysis crucially impacts
388 productive infection (47). Here, we now show that the IEC response indeed fuels the serine
389 pool via the glycolytic serine *de novo* synthesis pathways in order to sustain GSH synthesis
390 and maintain STING signalling. The functional outcome of increasing *de novo* serine synthesis
391 appears to be cell-type specific, as it has been previously shown that abrogation of *de novo*
392 serine synthesis via PHGDH exacerbates IFN-I signalling in macrophages via a mechanism

393 involving the YAP lysosomal degradation (48). Importantly, our data indicate that *de novo*
394 serine synthesis in IECs is primarily needed for glutathione synthesis and the reduction of
395 intracellular ROS, resulting in maintenance of STING signalling.
396 These findings might point to an important cell type-specific utilization of serine metabolism,
397 which is needed to contain CMV infections in the intestinal epithelium as the first line of
398 defence. Bearing in mind that the mechanical breakdown of the epithelial lining is a critical
399 hallmark of IBD, our data strongly put forward the idea of an ER-stress driven immune
400 exhaustion of the STING pathway in the intestinal epithelium as a critical layer of susceptibility
401 for CMV infection in IBD.

402 **Figure legends**

403 **Figure 1: Chronic ER-stress suppresses STING signalling in intestinal epithelial cells**
404 (A) *Xbp1*$^{fl/fl}$ (n= 13) and *Xbp1*$^{\Delta IEC}$ (n= 10) mouse small intestinal sections were stained for
405 STING, representative images. (B) Corresponding quantification of STING-positive cells per
406 crypt. (C) *Xbp1* fl/fl (n= 5) and *Xbp1*$^{\Delta IEC}$ (n= 5) mouse small intestinal crypts were isolated and
407 *Cxcl10* expression was assessed by q-RT-PCR. (D) iCtrl and i*Xbp1* Mode-K cells were
408 stimulated with DMXAA (100 µg/ml, 1 h) and protein expression assessed by Western Blot.
409 (E) *Cxcl10* and (F) *Ifnb* gene expression of Mode-K iCtrl and i*Xbp1* cells stimulated with
410 DMXAA (100 µg/ml, 3 h, n=3). (G) iCtrl and i*Xbp1* Mode-K cells were infected with MCMV
411 at a MOI of 10 and *Cxcl10* gene expression and (H) MCMV fold induction was assessed by
412 PCR (n= 4). (J) *Xbp1* fl/fl and *Xbp1*$^{\Delta IEC}$ mice were infected intraperitoneally with vehicle (n=11
413 for each group) or MCMV (n=12 (*Xbp1* fl/fl); n=14 (*Xbp1*$^{\Delta IEC}$)) and intestinal inflammation
414 was assessed. (K) representative images of HE stained small intestinal sections. Depicted data
415 representative of minimum of three independent experiments.

416 **Figure 2: ER-stress induces a distinct ROS-dependent metabolic adaptation to sustain**
417 **STING signalling**
418 (A) In vivo uptake of amino acids after 24h. Absolute consumption and release rates (CORE)
419 in fmol/PCV/h are displayed (n ≥ 3). (B) Relative intracellular metabolite level of iCtrl and
420 i*Xbp1* cells (n ≥ 3). Peak areas are normalized to PCV and internal standards. (C) Schematic
421 depicting of the GSH synthesis pathway. (GCL = glutamate-cysteine ligase; GS = glutathione
422 synthetase). (D-F) iCtrl and i*Xbp1* cells were treated with TM and CORE of (D) glutamate, (E)
423 cystine and (F) glycine was determined via GC-MS (n = 4, Two-way ANOVA). (G) Relative
424 *Slc7a11* mRNA expression of iCtrl and i*Xbp1* cells treated with (+) or without (-) TM (n = 3,
425 paired t-test). (H) Relative intracellular GSH level of iCtrl and i*Xbp1* cells (n = 9, paired t-test).
426 (I) GSH/GSSG ratios of iCtrl and i*Xbp1* cells (n =3, paired t-test). (J) Relative intracellular
427 ROS levels of iCtrl and i*Xbp1* cells treated with TM using DCF-DA (n ≥ 3, MFI ± SEM). (K)
428 Relative percentage of FITC+ cells in iCtrl and i*Xbp1* cells treated with 0.1 µg/ml TM for 24h
429 assessed by FACS (n =3). Depicted data representative of minimum of three independent
430 experiments.

431 **Figure 3: Serine and glutathione metabolism are critical gatekeepers of STING function**
432 **in intestinal epithelial cells**
433 (A) Schematic illustration of the different intervention strategies used to interfere with GSH
434 synthesis and GPX4 activity. (B) Relative intracellular serine level of iCtrl and i*Xbp1* cells in
435 medium lacking serine and glycine (-SG) in the presence (+) or absence (-) of 15 µM BI-4916
436 (n = 3) (C) Relative GSH level of iCtrl and i*Xbp1*cells in medium lacking serine and glycine (-
437 SG) treated with (+) or without (-) of 15 µM BI-4916 (n = 2). (D) Relative intracellular ROS
438 level of iCtrl and i*Xbp1* cells in medium lacking serine and glycine (-SG) treated with (+) or
439 without (-) of 15 µM BI-4916 (n ≥3. (E) Relative percentage of FITC+ cells in iCtrl and i*Xbp1*

440 cells treated with 0.1 µg/ml TM (n ≥ 3). (F) Mode-K iCtrl and i*Xbp1* cells were starved of
441 serine/glycine and treated with 15 µM BI for 24 h before stimulation with DMXAA (100 µg/ml,
442 3 h) and *Cxcl10* gene expression was analyzed by q-RT-PCR (n=3). (G) Western Blot of both
443 Mode-K iCtrl and i*Xbp1* cells stimulated with DMXAA (100 µg/ml, 1 h) after 24 h of SG
444 starvation and treatment with BI-4916 (15 µM). Depicted data representative of minimum of
445 three independent experiments.

446 **Figure 4: Restoration of glutathione function restores STING signalling and CMV**
447 **control in intestinal epithelial cells**

448 (A) Absolute consumption and release rates of glutamate in iCtrl and i*Xbp1* cells after NAC
449 treatment for 24h (n ≥ 3). (B) Relative intracellular ROS level of iCtrl and i*Xbp1* cells after
450 NAC treatment for 24 h (n ≥4, paired t-test). (C) Relative percentage of FITC+ cells in iCtrl
451 and i*Xbp1* cells after NAC treatment for 24h (n = 3, paired t-test). (D) Western Blot of both
452 Mode-K iCtrl and i*Xbp1* cells stimulated with DMXAA (100 µg/ml, 1 h) after 24 h of NAC
453 pretreatment (10 mM). (E) Western Blot of Mode-K iCtrl cells stimulated with DMXAA (100
454 µg/ml, 1 h) after 24 h pretreatment with NAC (10 mM) and RSL3 (0.5 µM). (F) q-RT-PCR of
455 *Cxcl10* (G) and *Ifnb1* expression from Mode-K iCtrl cells stimulated with DMXAA (100
456 µg/ml, 3 h) after 24 h of SG starvation and co-treatment with BI-4916 (15 µM) and NAC (10
457 mM) (n=3). (H) Western Blot of Mode-K iCtrl cells stimulated with DMXAA (100 µg/ml, 1
458 h) after 24 h of SG starvation and treatment with NAC (10 mM) and BI-4916 (15 µM). (I) q-
459 RT-PCR of *Cxcl10* expression from Mode-K iCtrl cells stimulated with DMXAA (100 µg/mL,
460 3 h) after 24 h of SG starvation and treatment with BI-4916 (15 µM) and NAC (10 mM) (n=4).
461 (J) Mode-K iCtrl and i*Xbp1* cells were stimulated with NAC (10mM) and infected MCMV. q-
462 RT-PCR of *Ifnb*, *Cxcl10* (K) and viral load as measured by viral DNA copy number (L) (n=4).
463 Depicted data representative of minimum of three independent experiments.

464 **Supplementary Figure 1: Chronic ER-stress abrogates intestinal epithelial STING**
465 **signalling**

466 (A) *Xbp1* fl/fl (n=2), STING -/- (n=1) and *Xbp1*$^{\Delta IEC}$ (n=2) mouse small intestinal crypts were
467 isolated and assessed for protein expression by Western Blot. (B) *Tmem173* and (C) *Ifnb1* gene
468 expression of *Xbp1* fl/fl (n=5) and *Xbp1*$^{\Delta IEC}$ (n=5) as assessed by q-RT-PCR. (D) iCtrl and
469 i*Xbp1* Mode-K cells were stimulated with dsDNA (1 µg/ml) for the indicated time and protein
470 concentration was assessed by Western Blot. (E) *Cxcl10* gene expression of the same
471 experiment as assessed by q-RT-PCR. (n=3). (F) Mode-K cells were subjected to either vehicle
472 or low-dose Tunicamycin (0,1 µg/ml) pretreatment, followed by dsDNA (1 µg/ml) stimulation.
473 Protein expression was assessed by Western Blot. (G) *Cxcl10* gene expression as assessed by
474 q-RT-PCR of the same experiment (n=4). (H) Mode-K iCtrl cells were subjected to *Tmem173*
475 knockdown by siRNA and subsequently stimulated with Tunicamycin (1 µg/ml) for the
476 indicated time-course and protein expression was analysed by Western blot. (I) Corresponding
477 gene expression analysis by q-RT-PCR (n=4). (J) *nATF6* VilCreERT2 tg or fl mice carrying a
478 Tamoxifen-inducible intestinal epithelial overexpression of ATF6, resulting in ER-stress
479 induction, were treated with Tamoxifen for 4d prior to sacrifice and STING expression was
480 assessed by immunohistochemistry. Representative HE/STING-stained small intestinal
481 sections. (K) Corresponding quantification of STING-positive cells per crypt (n=4 (fl) and n=6
482 (tg)). (L) *Ifnb* gene expression corresponding to Fig. 1G, H (n=4). (M) iCtrl or i*Xbp1* Mode-K
483 cells were exposed to *Listeria monocytogenes* at a MOI of 50 for 1 h before medium was
484 exchanged and Gentamicin (50 µg/ml) was added for 1 h, followed by Gentamicin at 5 µg/ml
485 for 22 h. *Cxcl10* and (N) *Ifnb* gene expression was assessed by q-RT-PCR (n=4). Depicted data
486 representative of three independent experiments.

487 **Supplementary Figure 2: Metabolic adaptations in response to ER-stress to maintain**
488 **redox balance**
489 (A) Schematic overview of the experimental workflow used to analyze metabolites from
490 medium and cell extracts. (B) Schematic illustration of the mass isotopomer distribution (MID)
491 of the TCA cycle from glucose. Filled red circle represent ^{13}C atoms derived from [U-^{13}C]
492 glucose. (C) Relative MIDs of the indicated TCA cycle intermediates in iCtrl or i*Xbp1* cells
493 cultured in [U-^{13}C] glucose medium for 24h. (D) Schematic illustration of the mass isotopomer
494 distribution (MID) of the TCA cycle from glutamine. Filled blue circle represent ^{13}C atoms
495 derived from [U-^{13}C] glutamine. (E) Relative MIDs of the indicated TCA cycle intermediates
496 in iCtrl or i*Xbp1* cells cultured in [U-^{13}C] glutamine medium for 24h. (F) Absolute consumption
497 and release rates of the indicated amino acids in organoids cultures derived from Xbp1 fl/fl
498 mouse small intestinal crypts after 24h. Representative experiment is shown. (G) Consumption
499 and release rates of serine in iCtrl and i*Xbp1* cells treated with TM for 24h ($n \geq 4$, Two-way
500 ANOVA). (H) Simplified illustration of the cellular GSH cycle (GR = glutathione reductase,
501 GPx = glutathione peroxidase genes). (I) Relative mRNA expression of the indicated GPx
502 genes in iCtrl and i*Xbp1* cells ($n = 4$, paired t-test). Depicted data representative of three
503 independent experiments.

504 **Supplementary Figure 3: Epithelial STING function relies on serine and gluthathione**
505 **metabolism**
506 (A-C) Relative intracellular metabolite level of (A) glycine, (B) serine and (C) γ-glutamyl-
507 cysteine (GGC) in iCtrl and i*Xbp1* cells cultured in complete or serine/glycine-free (-S/G)
508 medium for 24h ($n = 3$). (D) Fractional enrichment of serine M+3 in iCtrl and i*Xbp1* cells
509 cultured in complete or serine/glycine-free (-S/G) medium for 24h ($n =6$). (E) Fractional
510 enrichment of serine M+3 in iCtrl and i*Xbp1* cells cultured in complete or serine/glycine-free

511 (-S/G) medium in the presence (+) and absence (-) of 15 mM BI-4916 for 24h (n =3, two-way
512 ANOVA). Depicted data representative of three independent experiments.

513 **Supplementary Figure 4: Serine-glycine metabolism is increased in the intestinal**
514 **epithelium of IBD patients**
515 (A, B) ISG score and expression of serine pathway related genes in UC patients in GSE73661
516 (A) and GSE109142 (B) at timepoint 0. Red dots and connecting lines show the median
517 expression. (C, D) Correlation of serine pathway related genes with the ISG score in GSE73661
518 (C) and GSE109142 (D) in all available samples. The Pearson's correlation coefficients *r* and
519 p-values are shown. (E) ISG score and serine pathway related genes expression in GSE73661
520 patients according to therapy response (the latest available timepoint was analysed for each
521 patient). (F) Heatmap of ISG or Serine scores and *ATF4* expression in the main cell-types of
522 the SCP259 scRNA-Seq IBD dataset (colon mucosa of 18 UC patients and 12 healthy
523 individuals (45)). Colour shows z-scores and the dot size the percent of expressing cells. (G)
524 Heatmap of ISG or Serine scores and *ATF4* expression in selected epithelial cell clusters of
525 SCP259 in healthy (H), NI (non-inflamed) and inflamed (I) tissue biopsies. *p<0.05, **p<0.01,
526 ***p<0.001.

527 **<u>Methods</u>**

528 **Resource availability**

529 <u>Lead contact</u>
530 Further information and requests for resources and reagents should be directed to and will be
531 fulfilled by the lead contacts, Konrad Aden, MD (k.aden@ikmb.uni-kiel.de), Philip Rosenstiel,
532 MD (p.rosenstiel@mucosa.de) and Johannes Meiser, PhD (Johannes.Meiser@lih.lu).

533 Materials availability

534 This study did not generate new unique reagents.

535 Data and code availability

536 All data reported in this paper will be shared by the lead contact upon request.

537 This paper does not report original code.

538 Any additional information required to reanalyze the data reported in this paper is available

539 from the lead contact upon request.

540 **Experimental model and subject details**

541 Mice

542 *Xbp1* fl/fl mice were generated by targeted insertion of LoxP sites flanking the exon 2 of the

543 *Xbp1* gene. VillinCre+/- mice (strain: B6.SJL-Tg (Vil-cre)997Gum/J) were purchased from

544 Jackson Laboratory. Conditional knockout of *Xbp1* in the intestinal epithelium was then

545 established by crossing VillinCre+/- mice with *Xbp1* fl/fl mice, resulting in specific deletion of

546 *Xbp1* ($Xbp1^{\Delta IEC}$) in the intestinal epithelium (49). Tamoxifen-inducible nATF6-HA

547 overexpressing Villin-Cre n$Atf6^{IEC}$ mice (n*Atf6* VilCreERT2 transgene (tg)) mice were

548 generated as described previously (26). Overexpression of nATF6-HA was induced using

549 Tamoxifen for four days before sacrifice. *Tmem173* -/- mice were purchased from Jackson

550 Laboratory (previously described by Jin et al., 2011, strain #025805) (50).

551 Mice were housed under specific pathogen - free (SPF) conditions in individually ventilated

552 cages (IVCs). Animals were held in a 12 h light-dark cycle at 21 °C ± 2 °C and 60 % ± 5 %

553 humidity. Food and water were available ad libitum. All animal experiments were approved by

554 federal authorities and performed in accordance to institutional guidelines.

555 MCMV infection *in vivo*

556 For *in vivo* MCMV infection 8 week old *Xbp1* fl/fl and *Xbp1*$^{\Delta IEC}$ mice were infected
557 intraperitoneally with either 10^5 PFU MCMV or with vehicle. During the infection mice were
558 fed a standard chow diet and had free access to food and water. Five days after infection mice
559 were sacrificed and the intestines were harvested.

560 Cell culture

561 In this study, the SV40 large T-antigen-immortalized murine small intestinal epithelial cell line
562 MODE-K (51) was employed as an in vitro model for the intestinal epithelium. MODE-K cells
563 harbouring an RNA interference (RNAi) based knockdown of *Xbp1* and a control RNA
564 interference (i*Xbp1*, iCtrl) were kindly gifted by Artur Kaser, University of Cambridge (6). In
565 brief, RNA interference was achieved by stable introduction of a small hairpin RNA specific
566 for *Xbp1* and a control small hairpin RNA identical to Lee et al. (52), except that SFGΔU3hygro
567 was used. Knockdown of *Xbp1* was confirmed by qPCR. The following chemical stimulants
568 were used (name, company, catalogue-number): DMXAA/Vadimezan (Hölzel, HY-10964), N
569 Acetyl-L-cystein (Th. Geyer/Sigma, A7250-25G), BI-4916 (Hoelzel, HY-126253-5mg), RSL3
570 (Selleck Chemicals, S8155). siRNA knockdown of *Tmem173* was performed using the
571 Viromer® Blue kit (Lipocalyx, Halle, Germany) according to the manufacturer's protocol.
572 *Tmem173* siRNA was purchased from Qiagen (catalogue-number GS72512).

573 Organoid generation and handling

574 Mouse small intestinal organoids were cultivated as described previously (53,54). To generate
575 sustainable cultures of small intestinal organoids, mice were sacrificed and the small intestine
576 was removed and cut into pieces. PBS wit 10 nM EDTA was added to the pieces for 10 min
577 and the specimen was placed under mild agitation. Afterwards, the supernatant was removed,

578 fresh PBS/EDTA solution was added and incubated under mild agitation for 10 min again. This
579 was repeated four times. To remove debris, the suspension was filtered through a 100 µm
580 strainer and centrifuged at 1200 rpm for 10 min. Crypts were then either used for protein
581 respectively RNA isolation or resuspended in Matrigel and embedded in 24-well plates to
582 generate organoid cultures. Medium was changed twice per week. Organoids were stimulated
583 after 5 to 7 days of cultivation.

584 **Method details**

585 Histology

586 After sacrifice, the small intestine was removed and immediately fixed in 10 % (w/v) formalin
587 for 24 h at 4 °C. The tissue was then immersed in a series of ethanol solutions of increasing
588 concentrations until 100 %. Next, the ethanol was gradually replaced with xylene, which is
589 then replaced by paraffin. Paraffin embedded tissue was cut into 3.5-4.5 µm thin sections using
590 the RM2255 microtome. Paraffin embedded tissue sections were stained for 2-5 min in
591 haematoxylin. The cytoplasm was counterstained with 1 % (v/v) eosin solution for 2 min.
592 Stained slides were then dehydrated and embedded in Roti-Histo-Kit mounting medium and
593 examined with a Zeiss AxioImager.Z1 apotome microscope and the AxioVision Rel 4.9
594 software.

595 STING immunohistochemistry and quantification

596 To quantify STING expression in the intestinal epithelium, 3,3'-Diaminobenizidine staining
597 was performed. Slides were rehydrated and boiled for 20 min in citrate buffer (pH 6.0) for
598 antigen retrieval. Unspecific binding sites were blocked by incubating slides with 5 % (v/v)
599 goat serum in phosphate-buffered saline (PBS). Naturally occurring peroxidases were
600 inactivated by applying 3 % hydrogen peroxide. Antibody binding and 3,3'- diaminobenzidine

601 staining was performed according to the manufacturer's instruction (Vectastain Elite ABC Kit,
602 Vector Labs, Peterborough, United Kingdom). In brief, after primary antibody binding, the
603 signal was amplified by adding a horseradish peroxidase-conjugated streptavidin antibody.
604 Quantification was performed by counting average STING positive cells per crypt. For each
605 animal, 50 crypts were counted and averaged.

606 Western blot

607 Cells and tissues were lysed using 40-100 µl SDS-based DLB buffer + 1 % Halt™ Protease
608 inhibitor cocktail (ThermoFisher Scientific, Waltham, USA) before incubation for 5 minutes
609 at 95 °C followed by sonification for 2x 5 seconds. To remove cell remnants, lysates were
610 centrifuged at 16.000 x g for 15 minutes at 4°C and supernatants were transferred into a new
611 tube. For protein extraction of organoids, Matrigel™ was removed by incubation of organoids
612 in Corning™ Cell Recovery Solution (Corning, New York, USA) for 45-60 min at ice after
613 transferring organoids to tubes, centrifugation at 3000 g for 2 min and discarding supernatants.
614 Next, the lysis buffer as described above was added. The protein concentration was determined
615 applying the copper-based DC Protein Assay (Bio-Rad, Munich, Germany) according to the
616 manufacturer´s protocol. Proteins were separated by their molecular weight using precast
617 gradient polyacrylamide gels for improved separation of a wide range of proteins (NuPAGE®
618 4-12 % Bis-Tris gels, Life Technologies, Darmstadt, Germany). Protein lysates were prepared
619 by supplementation with the corresponding NuPAGE LDS Sample Buffer (Thermo Scientific,
620 Bremen, Germany), followed by incubation at 70 °C for 70 min. SDS-PAGE electrophoresis
621 was run at 160 V and a maximum current of 300 mA for 1 to 2 h in the XCell SureLock Mini
622 Cell system (Life Technologies, Darmstadt, Germany). NuPAGE MOPS SDS running buffer
623 was used to run the gels and Prestained PageRuler plus protein ladder 10-250 K (Thermo
624 Scientific, Bremen, Germany) served to estimate protein size. To detect proteins using
625 immunodetection by specific antibodies, separated proteins were transferred onto

626 polyvinylidene difluoride (PVDF) membranes. PVDF membranes (Bio-Rad, Munich,
627 Germany) were activated under mild agitation using methanol for 10 s, followed by 5 min of
628 washing in A. bidest. and then transferred for 5 min to anode buffer 1. Separated proteins were
629 transferred from the gel onto the membrane by semi-dry blotting using the Trans-Blot Turbo™
630 Transfer System (Bio-Rad, Munich, Germany) with a discontinuous buffer system consisting
631 of one cathode buffer and two anode buffers. Proteins were blotted onto the membrane at 0,3
632 A, 25 V for 60 min. After the transfer membranes were blocked with 5 % (w/v) blotting grade
633 blocker (non-fat dry milk) in Tris - buffered saline (TBS) supplemented with 0.1 % (v/v) Tween
634 20 (TBS - T) for 1 h. Membranes were probed with the appropriate primary and secondary
635 antibody. The primary antibody was applied in 5 % (w/v) blotting grade blocker (non-fat dry
636 milk) or bovine serum albumin (BSA) in Tris-buffered saline (TBS) supplemented with 0.1 %
637 (v/v) Tween 20 according to the manufacturer's instruction and incubated overnight at 4 °C
638 under mild shaking. Next, the membrane was washed three times with TBS - T for 15 min to
639 remove excess antibody. A horseradish peroxidase (HRP) conjugated secondary antibody was
640 diluted in 5 % (w/v) blotting grade blocker (non-fat dry milk) in TBS-T according to the
641 manufacturer's recommendation and incubated for 1 h at room temperature. Binding of the
642 secondary antibody was detected using a chemiluminescent substrate kit (Thermo Scientific)
643 and recorded with an automated developer machine (Agfa, Mortsel, Belgium). The following
644 antibodies were used: Actin β (Sigma-Aldrich, Munich, Germany, A-5441), β-Tubulin (MBL
645 International, Woburn, USA, M150-3), phospho-STING (Cell Signalling Technology, Leiden,
646 The Netherlands, 72971), phospho-TBK1 (Cell Signalling Technology, Leiden, The
647 Netherlands, 5483), STING (Cell Signalling Technology, Leiden, The Netherlands, 13647),
648 TBK1 (Cell Signalling Technology, Leiden, The Netherlands, 38066), mouse-HRP
649 (Amersham Biosciences, Glattbrugg, Switzerland, NA931V), rabbit-HRP (Amersham
650 Biosciences, Glattbrugg, Switzerland, NA934V).

651 q-RT-PCR

652 RNA extraction was performed using the RNeasy Mini Kit (Qiagen, Hilden, Germany)
653 according to the manufacturer's instruction. To generate cDNA, 100-1000 ng total RNA
654 (depending on the amount of previously extraced RNA) was transcribed into complementary
655 DNA (cDNA) by reverse transcription using the Maxima H Minus First Strand cDNA
656 Synthesis Kit (Thermo Scientific, Bremen, Germany). Reverse transcription was performed
657 following the manufacturer´s instruction. Quantitative real-time PCRs (q-RT-PCR) was used
658 to amplify and simultaneously quantify mRNA levels using target-specific oligonucleotides.
659 Predesigned TaqMan probes (Applied Biosystems, Carlsbad, USA were purchased and used.
660 The 7900HT Fast Real Time PCR System (Applied Biosystems, Darmstadt, Germany) was
661 used for qPCR experiments. Samples were run in duplicates on 384-well plates. For the PCR
662 reaction, 5-10 ng cDNA and 0,5 µl of the respective TaqMan gene expression assays were used.
663 The PCR program was carried out following the manufacturer's recommendation (TaqMan
664 Gene Expression Master Mix protocol, Applied Biosystems, Darmstadt, Germany).
665 Alternatively, RT-qPCR was performed from 10 ng cDNA per sample using Fast SYBR™
666 Green Master Mix (Lifetech) at 95°C for 20 s, 40 cycles of 95°C for 1 s and 60°C for 20 s on
667 the QuantStudio 5 Real-Time PCR System (ThermoFisher). Relative quantification of each
668 gene was done by QuantStudio Design&Analysis v1.5.1 software (ThermoFisher) and
669 comparative Ct method. All samples were analysed in technical duplicates and repeat as
670 independent, biological experiments ($n \geq 3$). Moreover, all expression data were normalized to
671 housekeeping genes (*Tbp*, *Hrpt1* or *Actinb*). Taqman assay probes were purchased from Life
672 Technologies, Darmstadt, Germany (*Cxcl10*, 04331182; *Gapdh*, 99999915; Ifnb1, 04331182;
673 *Tmem173*, 04331182; *Xbp1*, 03464496). All non-TaqMan assay mouse primers used in this
674 study can be found in the table below:

Gene name	Forward primer sequence ((5' – 3')	Reverse primer sequence(5' – 3')

Slc7a11	GCTCGTAATACGCCCTGGAG	GGAAAATCTGGATCCGGGCA
Gpx1	ACCGTGTATGCCTTCTCCGC	CTCGGTGTAGTCCCGGATCG
Gpx2	AGTTCGGACATCAGGAGAACTG	GATGCTCGTTCTGCCCATTG
Gpx3	ACAATTGTCCCAGTGTGTGCAT	TGGACCATCCCTGGGTTTC
Gpx4	CATTGGTCGGCTGCGTGA	CGCGGGATGCACACATGG
Tbp	GTCATTTTCTCCGCAGTGCC	GCTGTTGTTCTGGTCCATGAT
Hrpt1	TGGATACAGGCCAGACTTTGTT	CAGATTCAACTTGCGCTCATC

675

676 Listeria monocytogenes infection

677 *Listeria monocytogenes* serotype 1/2a strain EGD was used to test type I IFN induction in
678 MODE-K cells. Bacteria were plated out from glycerol stocks onto brain-heart infusion (BHI;
679 BD Biosciences, Franklin Lakes, USA) agar plates overnight. *Listeria* colonies were then
680 transferred into 1 ml BHI medium and incubated overnight at 37 °C to allow for bacterial
681 replication. Next, bacteria were diluted and reincubated at 37 °C to induce a log - phase growth
682 until OD600 = 0.6 was reached. After washing with PBS, bacteria were diluted in MODE-K
683 medium and added to the cells according to multiciply of infection (MOI). As described
684 previously (55), MODE-K cells were infected at a MOI of 50. After allowing bacterial invasion
685 for 1 h, the bacteria-containing medium was removed, cells were washed once with PBS and
686 then treated with gentamicin (50 µg/ml) for 1 h to kill extracellular bacteria. The gentamicin-
687 containing medium was then replaced with medium containing a lower concentration of
688 Gentamicin (5 µg/ml), and cells were lysed for protein and RNA harvesting after another 22 h.

689 MCMV infection and quantification of replication

690 MCMV was prepared as described previously (56) and infection of MODE-K cells was
691 performed at a MOI of 10. Fold induction of MCMV was quantified by RT-PCR using the
692 MCMV M54 gene sequence: ATCATCCGTTGCATCTCGTTG (forward),
693 CGCCATCTGTATCCGTCCAT (reverse).

694 Histology score CMV colitis

695 After staining, an expert pathologist assessed inflammation with a semi quantitative scoring
696 system as previously reported (5). To assess the inflammation five subscores are summed up
697 for every sample and multiplied by the extent of the affected area (1, <10%; 2, 10%-25%; 3,
698 25%-50%; 4, >50% of the intestine affected). As subscores the following parameters are used:
699 mononuclear infiltrate (0: absent; 1: mild, 2: moderate 3: severe), crypt hyperplasia, epithelial
700 injury/erosion, polymorphonuclear infiltrate and transmural inflammation.

701 Flow Cytometric Analysis of ROS Levels

702 250,000 iCtrl or i*Xbp1* Mode-K cells were seeded in six-well plates and treated the subsequent
703 day as indicated in the figure legends. After an incubation time of 24h, cells were stained with
704 Zombie NIR (BioLegend, 1:1000 diluted in PBS) for 20 min at 37°C (to discriminate live and
705 dead cells in the later analysis), detached with trypsin, centrifuged at 350 g for 5 min and
706 washed with warm DMEM. Then, cells were stained in 100 µl DMEM supplemented with
707 10 µM DCF-DA (PromoCell) for 30 min at 37°C. After the incubation step, cells were
708 centrifuged at 350 g for 5 min, washed twice with ice-cold PBS and resuspended in ice-cold
709 FACS buffer (PBS with 10 % FBS and 0.5 mM EDTA). Samples were measured using the BD
710 FACSCanto™ system and BD FACSDiva software. Data analysis was performed using
711 FlowJo v10.6.2 software. All measurements were performed as independent, biological
712 experiments ($n \geq 3$) indicated in the respective figure legend.

713 Flow Cytometric Analysis of LPO Levels

714 Image-iT™ Lipid Peroxidation Kit (ThermoFisher) was used according to manufacturer`s
715 instructions. In brief, 250,000 iCtrl or i*Xbp1* Mode-K cells were cultivated in 2 ml medium and
716 treated after 24h as stated in the figure legends. Following 24h incubation, cells were harvest
717 via trypsinization, centrifuged at 350 g for 5 min and washed with warm DMEM. Then, cells

718 were stained in 100 µl DMEM supplemented with 10 µM Lipid peroxidation sensor
719 (BODIPY® 581/591 C11) for 30 min at 37°C. After two washing steps with ice-cold PBS at
720 350 g for 5 min, cells were resuspended in ice-cold 400 µl FACS buffer and measured using
721 NovoCyte Quanteon system (Aligent). Data analysis was performed using FlowJo v10.6.2
722 software. All measurements were performed as independent, biological experiments ($n \geq 3$).

723 Determination of GSH/GSSG ratio

724 GSH/GSSG ratios were obtained via a GSH/GSSG-GLO™ assay kit (Promega, V6611)
725 following the manufacturer`s instructions. For the experiments, $4x10^4$ iCtrl or iXbp1 cells were
726 plated out in opaque, white 96 well plates (Greiner, CELLSTAR, 655083), incubated for 24h
727 in DMEM (10% FBS) and processed according to the manufacture`s protocol. GSH/GSSG
728 ratios were determine by the following equation: total GSH-(GSSGx2)/GSSG. All
729 measurements were performed as technical replicates (N = 3) and repeated as independent,
730 biological experiments (n = 3) indicated in the respective figure legend.

731 Stable isotope tracing and metabolite extraction

732 Stable isotope tracing experiments were performed as previously described in Kiweler *et al.*,
733 2020 (57). Briefly, [U-^{13}C]-glucose or [U-^{13}C]-glutamine (Cambridge Isotope Laboratories,
734 CLM-1396 and CLM-1822) tracing was performed in DMEM supplemented with 10 % FBS
735 and the respective tracers (2 mM glutamine or 17 mM glucose). $2x10^5$ cells were seeded in 12-
736 well plates in triplicates for each experimental condition. Furthermore, an identical set of
737 triplicate wells were plate-out to calculate the packed cell volume (PCV) by determining cell
738 count and cell volume at the start and end of each tracing experiment (42). After 24h, growth
739 medium was replaced by ^{13}C tracer medium and cells were cultured for an additional 24 h at
740 37°C. In parallel, starting PCV was determined by counting three wells per condition. To assess
741 PCV at the end of the experiment, one set of triplicate wells was counted at the experimental

742 endpoint, whereas another triplicates set was used for subsequent metabolite extraction. In
743 addition, medium was collected, centrifuged at 350 g for 10 min at 4°C and supernatants were
744 stored at -80°C until medium quantification via GC-MS or YSI.
745 For GC-MS analysis, cells from [U-^{13}C]-glucose and [U-^{13}C]-glutamine tracer experiments
746 were washed once with 0.9 % ice-cold NaCl. Thereafter, metabolites were extracted by adding
747 400 µl ice-cold MeOH/mqH_2O (ratio, 1:1) to each well. In addition, the extraction solvent
748 contains the internal standards pentanedioc-d6 acid and [U-^{13}C]-ribitol at a final concentration
749 of 1 µg/ml as well as Tridecanoid-d25 acid at a final concentration of 5 µg/ml. After the plates
750 were incubated for 5 min at 4°C on a rocking shaker, supernatant was transferred to 1.5-ml
751 Eppendorf tubes, mixed with 200 µl $CHCl_3$, and centrifuged for 5 min at 13,000 g and at 4°C.
752 Finally, the upper polar phase was collected, fully dried via SpeedVac and stored at -20°C for
753 subsequent GC-MS analysis.
754 For LC-MS analysis, metabolites extraction was performed as previously described by Meiser
755 *et al*., 2016 (42) and extracted metabolites were stored at -80°C until LC-MS analysis.

756 <u>GC-MS: Determination of MIDs of intracellular metabolites following stable isotope tracing</u>
757 Polar metabolites were derivatized for 90 min at 55 °C with 20 µl of methoxyamine (c = 20
758 mg/ml) in pyridine under continuous shaking and subsequently for 60 min at 55 °C with 20 µl
759 of MTBSTFA w/ 1% TBDMCS. GC-MS analysis was performed using an Agilent 7890B GC
760 coupled to an Agilent 5977A Mass Selective Detector (Agilent Technologies). A sample
761 volume of 1 µl was injected into a Split/Splitless inlet, operating in splitless mode at 270 °C.
762 Gas chromatograph was equipped with a 30 m (I.D. 250 µm, film 0.25 µm) ZB-35MS capillary
763 column with 5 m guard column (Phenomenex). Helium was used as carrier gas with a constant
764 flow rate of 1.2 ml/min. GC oven temperature was held at 100 °C for 2 min and increased to
765 300 °C at 10 °C/min and held for 4 min. Total run time was 26 min. Transfer line temperature
766 was set to 280 °C. Mass selective detector (MSD) was operating under electron ionization at

767 70 eV. MS source was held at 230 °C and the quadrupole at 150 °C. For precise quantification
768 of the MID, measurements were performed in selected ion monitoring mode. Target ions (m/z)
769 and Dwell times are shown in Table 2.
770 The MetaboliteDetector software package (v. 3.220180913) was used for mass spectrometric
771 data post processing, quantification, MID calculations, correction of natural isotope abundance,
772 and determinations of fractional carbon contributions (58).
773
774 **Table 2:** Target ions and Dwell times of metabolites quantified in this study.

Derivative (m/z of selected fragment)	Quant-Ions (m/z)	Dwell Time (ms/ for each)	Sum Formula (fragment)	MID size
Pyruvic Acid 1MeOX 1TBDMS (174)	174.0 – 180.1	15	C6H12O3NSi	4
Lactic acid 2TBDMS (261)	261.1 – 267.1	15	C11H25O3Si2	4
Alanine 2TBDMS (260)	260.1 – 266.1	15	C11H26NO2Si2	4
Glycine 2TBDMS (246)	246.1 – 252.1	15	C10H24NO2Si2	3
Valine 2TBDMS (288)	288.2 – 295.2	15	C13H30NO2Si2	6
Leucine 2TBDMS (302)	302.2 – 310.2	15	C14H32NO2Si2	7
Isoleucine 2TBDMS (302)	302.2 – 310.2	15	C14H32NO2Si2	7
Proline 2TBDMS (286)	286.2 – 294.2	15	C13H28NO2Si2	6
Succinic Acid 2TBDMS (289)	289.1 – 296.1	15	C12H25O4Si2	5
Fumaric Acid 2TBDMS (287)	287.1 – 294.1	15	C12H23O4Si2	5
(Internal Standard) Pentanedioic-D6 Acid	235.2, 309.2, 351.3	30		
Serine 3TBDMS (390)	390.2 – 396.2	15	C17H40NO3Si3	4
Methionine 2TBDMS (320)	320.2 – 328.2	10	C13H30NO2SSi2	6
a-Ketoglutaric Acid 1MeOX 2TBDMS (346)	346.2 – 354.2	10	C14H28NO5Si2	6
Malic Acid 2TBDMS (419)	419.2 – 426.2	15	C18H39O5Si3	5
Aspartic Acid 3TBDMS (418)	418.2 – 425.2	15	C18H40NO4Si3	5
Glutamic Acid 3TBDMS (432)	432.3 – 440.3	10	C19H42NO4Si3	6
Lysine 3TBDMS (431)	431.3 – 440.3	15	C20H47N2O2Si3	7
Glutamine 3TBDMS (431)	431.3 – 439.3	10	C19H43N2O3Si3	6
Citric Acid 4TBDMS (591)	591.3 – 600.3	10	C26H55O7Si4	7

3-Phosphoglyceric acid 4TBDMS (585)	585.4 – 592.4	15	C27H63O7PSi4	4
Histidine 3TBDMS (440)	440.2 – 449.2	15	C20H42N3O2Si3	7
Tryptophan 2TBDMS (375)	375.2 – 389.2	10	C19H31N2O2Si2	12

775

776 Analysis of Medium Exchange Rates

777 Medium quantification and exchange rate calculation was performed as described in Meiser et
778 al., 2016 (42). For metabolite extraction, 20 µl of the collected medium sample was mixed with
779 180 µl extraction solvent (80 % MeOH/20 % mqH_2O) containing the internal standards [U-
780 13C]-ribitol (50 µg/ml) and pentanedioc-d6 acid (20 µg/ml), vortexed for 10 s and
781 subsequently incubated for 15 min at 4°C and 1350 rpm in a thermomixer. After centrifugation
782 for 5 min at max speed, 50 µl of the supernatant was transferred in GC-vial and dried on
783 SpeedVac overnight.

784 Metabolite derivatization was performed by using a multi-purpose sample preparation robot
785 (Gerstel). Dried medium extracts were dissolved in 30 µl pyridine, containing 20 mg/mL
786 methoxyamine hydrochloride (Sigma-Aldrich), for 120 min at 45 °C under shaking. After
787 adding 30 µl N-methyl-N-trimethylsilyl-trifluoroacetamide (Macherey-Nagel), samples were
788 incubated for 30 min at 45 °C under continuous shaking.

789 GC-MS analysis was performed by using an Agilent 7890A GC coupled to an Agilent 5975C
790 inert XL Mass Selective Detector (Agilent Technologies). A sample volume of 1 µl was
791 injected into a Split/Splitless inlet, operating in split mode (10:1) at 270 °C. The gas
792 chromatograph was equipped with a 30 m (I.D. 0.25 mm, film 0.25 µm) DB-5ms capillary
793 column (Agilent J&W GC Column) with 5 m guard column in front of the analytical column.
794 Helium was used as carrier gas with a constant flow rate of 1.2 ml/min. The GC oven
795 temperature was held at 90 °C for 1 min and increased to 220 °C at 10 °C/min. Then, the
796 temperature was increased to 280 °C at 20 °C/min followed by 5 min post run time at 325 °C.

797 The total run time was 22 min. The transfer line temperature was set to 280 °C. The MSD was
798 operating under electron ionization at 70 eV. The MS source was held at 230 °C and the
799 quadrupole at 150 °C. Mass spectra were acquired in selected ion monitoring (SIM) mode for
800 precise quantification of medium components. In Table 3, masses used for quantification and
801 qualification of the derivatized target analytes (dwell times between 25 and 70 ms) are
802 illustrated.
803
804 **Table 3**: List of quantification and qualification ions used for metabolite detection in medium.

Analyte Name	Quantification Ions (*m/z*)	Qualification Ion I (m/z)	Qualification Ion II (m/z)
Pyruvic acid 1MEOX 1TMS	174-179	158.1	189.1
Lactic acid 2TMS	219.1-224.1	190.1	117.1
Alanine 2TMS	218.1-223.1	190.1	116.1
Valine 2TMS	144.1	218.1	246.2
Leucine 2TMS	158.1	218.1	232.2
Isoleucine 2TMS	158.1	218.1	232.2
Glycine 3TMS	276.1-280.1	248.1	174
Serine 3TMS	306.1-311.1	218.1	204.1
Threonine 3TMS	218.1	291.2	320.2
IS Pentanedioic acid-D6 2TMS	267.1	163.1	239.1
Methionine 2TMS	176.1	250.1	293.1
Glutamic acid 3TMS	363.2-371.2	246.1	348.2
Phenylalanine 2TMS	192.1	218.1	266.1
Asparagine 3TMS	231.1-236.1	132.1	348.1
IS [UL-13C5]-Ribitol 5TMS	220.1	310.2	323.2
Glutamine 3TMS	347.2-354.2	245.1	156.1
Glucose 1MEOX 5TMS	319.2, 323.2	217.1	220.1
Lysine 4TMS	174.1	317.2	434.3
Tyrosine 3TMS	218.1	179.1	280.2
Tryptophan 2TMS	218.1-223.1	130	348.2
Cystine 4TMS	218.1-223.1	297.1	411.2

805
806 All GC-MS chromatograms were processed using MetaboliteDetector (v. 3.2.20190704).
807 Compounds were annotated by retention time and mass spectrum using an in-house mass
808 spectral (SIM) library (overall similarity: >0.60). The following deconvolution settings were
809 applied: Peak threshold: 2; Minimum peak height: 2; Bins per scan: 10; Deconvolution width:

810 8 scans; no baseline adjustment; Minimum 1 peaks per spectrum; no minimum required base
811 peak intensity.
812 Peak areas of all isotopologues of defined quantification ions were summed up and divided by
813 the peak area of the internal standard for normalization. In addition, a calibration curve was
814 prepared to calculate absolute concentrations. Absolute uptake and release rates were
815 calculated as described in Hiller et al. 2009 (58).

816 LC-MS measurements

817 Untargeted LC-MS analysis was carried out as previously (42). For calculating intracellular
818 metabolite level, measured peak areas were initially corrected for natural isotope abundance,
819 normalized to internal standards and subsequently divided by PCV to obtain relative metabolite
820 levels.

821 YSI measurements

822 Collected medium samples were initially filtrated (Phenex-RC 4mm Syringe Filters 0.2 µm)
823 prior measurement to remove particles. Absolute quantitative values for Glutamine and
824 Glutamic acid were acquired using the YSI 2950D Biochemistry Analyzer (Kreienbaum
825 KWM). For a precise and reliable quantification, external calibration curves of each compound
826 were prepared and measured in duplicates. To get absolute consumption and release rate
827 (CORE, fmol/PCV/h), measured concentrations were divided by PCV (determined at start and
828 end of the experiment, see stable isotope tracing for details) and the duration of the experiment.

829 IFN and Serine related genes in IBD bulk and scRNA-Seq datasets

830 The publicly available GSE109142 (59) (RNA sequencing TPM counts of pediatric ulcerative
831 colitis patients) and GSE73661 (60) (microarray of UC patients treated with either infliximab
832 or vedolizumab) were downloaded from the Gene Expression Omnibus (GEO) repository and

833 processed using *R* version 4.1.0. TPM counts were log2 transformed after adding half of the
834 smallest non-zero value.
835 Digital gene expression matrices for SCP259 (45) (colon mucosa of 18 UC patients and 12
836 healthy individuals) were downloaded from the Single Cell Portal and processed in *R* using the
837 Seurat package. Following UMAP dimensional reduction, cells were clustered using the
838 FindClusters() function in Seurat at a resolution of 0.5. Main cell types were labelled using the
839 SingleR package and the Encode+Blueprint reference dataset. Epithelial cells were further
840 subclustered at a resolution of 0.5 and the 24 identified clusters labelled using known epithelial
841 markers published by Elmentaite et al., 2021 (61). Cells extracted from the lamina propria were
842 considered for subsequent analyses.
843 Gene expression scores were calculated as the mean of scaled and centered expression values
844 (z-scores) for the bulk datasets or on the mean normalized counts for the scRNA-Seq dataset.
845 ISG composing signature genes were *IFITM1*, *MX1*, *OAS3*, *IFIT1*, *IFI44L* and *IFI16* as
846 previously described (23). The serine score was calculated on the serine pathway related genes
847 *PHGDH*, *MTHFD2*, *SHMT2*, *MTHFD1L* and *SLC7A11*.

848 **Quantification and statistical analysis**

849 The GraphPad Prism 5 software package (GraphPad Software Inc., La Jolla, USA) was used
850 for statistical analysis. If not otherwise specified, the Student's unpaired t-test was performed.
851 Data is visualized as mean ± standard error of the mean (SEM), if not otherwise stated. A
852 significance threshold of a p-value ≤ 0.05 (*) was used, a p-value of ≤ 0.01, respectively ≤
853 0.001, were considered as strongly significant (**) and highly significant (***), if not
854 otherwise specified.
855 We define one *n* as one independent biological experiment (in some cases further consisting of
856 several wells, e.g. triplicate wells for all stable isotope tracing experiments). The technical

857 mean of one biological experiment was considered as one *n*. The mean values of several
858 independent, biological experiments (as indicated in figure legends) were plotted and used for
859 statistical analysis as indicated.

860 **Funding & Acknowledgement**

861 This work was supported by the DFG Research Training Group 1743 (P.R.), the BMBF
862 iTREAT project (P.R.), DFG Cluster of excellence "Precision medicine in chronic
863 inflammation" RTF III and TI-1, the DFG CRC 1182 C2 (P.R.) the EKFS research grant
864 #2019_A09 (K.A.), the Wilhelm Sander-Stiftung #2019.046.1 (K.A.), the BMBF (eMED
865 Juniorverbund "Try-IBD" 01ZX1915A), the DFG RU5042 (P.R., K.A.), the FNR-ATTRACT
866 program A18/BM/11809970 (J.M.), the "European Union under the Horizon 2020 Research
867 and Innovation Program" (S.J.W) and the MSCA-Innovative Training Networks Programme
868 MSCA-ITN (EDGE, 675278) (S.J.W.). Stable isotope tracers were provided as part of a
869 Research Award by Cambridge Isotope Laboratories Inc. (B.B. and J.M.).
870 We thank M. Rohm, M. Hansen, S. Kock, D. Oelsner, S. Baumgarten, M. Reffelmann, J.
871 Ohrndorf for perfect technical assistance. We also thank the LCSB Metabolomics Platform,
872 especially Xiangyi Dong and Floriane Vanhalle, for providing technical and analytical support;
873 the National Cytometry Platform (Quantitative Biology Unit, LIH) and especially Thomas
874 Cerutti for support with flow cytometric analyses.

875 **References**

876 1. Kaplan GG. The global burden of IBD: from 2015 to 2025. Nat Rev Gastroenterol
877 Hepatol. 2015 Dec;12(12):720–7.
878 2. Schenk W, Klugmann T, Borkenhagen A, Klecker C, Dietel P, Kirschner R, et al. The
879 detection of the cytomegalovirus DNA in the colonic mucosa of patients with ulcerative colitis
880 is associated with increased long-term risk of proctocolectomy: results from an outpatient IBD

881 clinic. Int J Colorectal Dis. 2019 Mar;34(3):393–400.
882 3. Qin Y, Wang G, Kong D, Li G, Wang H, Qin H, et al. Risk Factors of Cytomegalovirus
883 Reactivation in Ulcerative Colitis Patients: A Meta-Analysis. Diagn Basel Switz. 2021 Oct
884 21;11(11):1952.
885 4. Grootjans J, Kaser A, Kaufman RJ, Blumberg RS. The unfolded protein response in
886 immunity and inflammation. Nat Rev Immunol. 2016 Aug;16(8):469–84.
887 5. Adolph TE, Tomczak MF, Niederreiter L, Ko HJ, Böck J, Martinez-Naves E, et al.
888 Paneth cells as a site of origin for intestinal inflammation. Nature. 2013 Nov;503(7475):272–
889 6.
890 6. Kaser A, Lee AH, Franke A, Glickman JN, Zeissig S, Tilg H, et al. XBP1 Links ER
891 Stress to Intestinal Inflammation and Confers Genetic Risk for Human Inflammatory Bowel
892 Disease. Cell. 2008 Sep 5;134(5):743–56.
893 7. Heazlewood CK, Cook MC, Eri R, Price GR, Tauro SB, Taupin D, et al. Aberrant
894 Mucin Assembly in Mice Causes Endoplasmic Reticulum Stress and Spontaneous
895 Inflammation Resembling Ulcerative Colitis. PLOS Med. 2008 Mar 4;5(3):e54.
896 8. Tréton X, Pédruzzi E, Cazals–Hatem D, Grodet A, Panis Y, Groyer A, et al. Altered
897 Endoplasmic Reticulum Stress Affects Translation in Inactive Colon Tissue From Patients
898 With Ulcerative Colitis. Gastroenterology. 2011 Sep 1;141(3):1024–35.
899 9. Zhao F, Edwards R, Dizon D, Afrasiabi K, Mastroianni JR, Geyfman M, et al.
900 Disruption of Paneth and goblet cell homeostasis and increased endoplasmic reticulum stress
901 in Agr2−/− mice. Dev Biol. 2010 Feb 15;338(2):270–9.
902 10. Stengel S, Messner B, Falk-Paulsen M, Sommer N, Rosenstiel P. Regulated proteolysis
903 as an element of ER stress and autophagy: Implications for intestinal inflammation. Biochim
904 Biophys Acta BBA - Mol Cell Res. 2017 Nov 1;1864(11):2183–90.
905 11. Vanhove W, Nys K, Arijs I, Cleynen I, Noben M, De Schepper S, et al. Biopsy-derived

906 Intestinal Epithelial Cell Cultures for Pathway-based Stratification of Patients With
907 Inflammatory Bowel Disease. J Crohns Colitis. 2018 Jan 24;12(2):178–87.
908 12. Powell N, Pantazi E, Pavlidis P, Tsakmaki A, Li K, Yang F, et al. Interleukin-22
909 orchestrates a pathological endoplasmic reticulum stress response transcriptional programme
910 in colonic epithelial cells. Gut. 2020 Mar;69(3):578–90.
911 13. Welz L, Kakavand N, Hang X, Laue G, Ito G, Silva MG, et al. Epithelial X-Box Binding
912 Protein 1 Coordinates Tumor Protein p53-Driven DNA Damage Responses and Suppression
913 of Intestinal Carcinogenesis. Gastroenterology. 2022 Jan;162(1):223-237.e11.
914 14. Tschurtschenthaler M, Adolph TE, Ashcroft JW, Niederreiter L, Bharti R, Saveljeva S,
915 et al. Defective ATG16L1-mediated removal of IRE1α drives Crohn's disease–like ileitis. J
916 Exp Med. 2017 Feb 1;214(2):401–22.
917 15. Motwani M, Pesiridis S, Fitzgerald KA. DNA sensing by the cGAS–STING pathway
918 in health and disease. Nat Rev Genet. 2019 Jul 29;1–18.
919 16. Hopfner KP, Hornung V. Molecular mechanisms and cellular functions of cGAS–
920 STING signalling. Nat Rev Mol Cell Biol. 2020 May 18;1–21.
921 17. Wottawa F, Bordoni D, Baran N, Rosenstiel P, Aden K. The role of cGAS/STING in
922 intestinal immunity. Eur J Immunol. 2021;51(4):785–97.
923 18. Lio CWJ, McDonald B, Takahashi M, Dhanwani R, Sharma N, Huang J, et al. cGAS-
924 STING Signaling Regulates Initial Innate Control of Cytomegalovirus Infection. J Virol. 2016
925 Sep 1;90(17):7789–97.
926 19. Piersma SJ, Poursine-Laurent J, Yang L, Barber GN, Parikh BA, Yokoyama WM. Virus
927 infection is controlled by hematopoietic and stromal cell sensing of murine cytomegalovirus
928 through STING. eLife. 2020 Jul 29;9.
929 20. Stempel M, Chan B, Juranić Lisnić V, Krmpotić A, Hartung J, Paludan SR, et al. The
930 herpesviral antagonist m152 reveals differential activation of STING-dependent IRF and NF-

931 κB signaling and STING's dual role during MCMV infection. EMBO J. 2019 Mar
932 1;38(5):e100983.
933 21. Guimarães ES, Gomes MTR, Campos PC, Mansur DS, Dos Santos AA, Harms J, et al.
934 Brucella abortus Cyclic Dinucleotides Trigger STING-Dependent Unfolded Protein Response
935 That Favors Bacterial Replication. J Immunol Baltim Md 1950. 2019 May 1;202(9):2671–81.
936 22. Moretti J, Roy S, Bozec D, Martinez J, Chapman JR, Ueberheide B, et al. STING
937 Senses Microbial Viability to Orchestrate Stress-Mediated Autophagy of the Endoplasmic
938 Reticulum. Cell. 2017 Nov 2;171(4):809-823.e13.
939 23. Aden K, Tran F, Ito G, Sheibani-Tezerji R, Lipinski S, Kuiper JW, et al. ATG16L1
940 orchestrates interleukin-22 signaling in the intestinal epithelium via cGAS–STING. J Exp Med.
941 2018 Nov 5;215(11):2868–86.
942 24. Isler JA, Skalet AH, Alwine JC. Human Cytomegalovirus Infection Activates and
943 Regulates the Unfolded Protein Response. J Virol. 2005 Jun;79(11):6890–9.
944 25. Stengel ST, Fazio A, Lipinski S, Jahn MT, Aden K, Ito G, et al. Activating
945 Transcription Factor 6 Mediates Inflammatory Signals in Intestinal Epithelial Cells Upon
946 Endoplasmic Reticulum Stress. Gastroenterology. 2020 Jul;S0016508520349246.
947 26. Coleman OI, Lobner EM, Bierwirth S, Sorbie A, Waldschmitt N, Rath E, et al.
948 Activated ATF6 Induces Intestinal Dysbiosis and Innate Immune Response to Promote
949 Colorectal Tumorigenesis. Gastroenterology. 2018 Nov 1;155(5):1539-1552.e12.
950 27. Dambacher J, Beigel F, Seiderer J, Haller D, Goke B, Auernhammer CJ, et al.
951 Interleukin 31 mediates MAP kinase and STAT1/3 activation in intestinal epithelial cells and
952 its expression is upregulated in inflammatory bowel disease. Gut. 2007 Apr 5;56(9):1257–65.
953 28. Onyeagocha C, Hossain MS, Kumar A, Jones RM, Roback J, Gewirtz AT. Latent
954 cytomegalovirus infection exacerbates experimental colitis. Am J Pathol. 2009
955 Nov;175(5):2034–42.

956 29. Hansen K, Prabakaran T, Laustsen A, Jørgensen SE, Rahbæk SH, Jensen SB, et al.
957 Listeria monocytogenes induces IFNβ expression through an IFI16-, cGAS- and STING-
958 dependent pathway. EMBO J. 2014 Aug 1;33(15):1654–66.
959 30. Zhang J, Pavlova NN, Thompson CB. Cancer cell metabolism: the essential role of the
960 nonessential amino acid, glutamine. EMBO J. 2017 May 15;36(10):1302–15.
961 31. Meister A. New aspects of glutathione biochemistry and transport--selective alteration
962 of glutathione metabolism. Nutr Rev. 1984 Dec;42(12):397–410.
963 32. Chen Y, Shertzer HG, Schneider SN, Nebert DW, Dalton TP. Glutamate cysteine ligase
964 catalysis: dependence on ATP and modifier subunit for regulation of tissue glutathione levels.
965 J Biol Chem. 2005 Oct 7;280(40):33766–74.
966 33. Bannai S, Sato H, Ishii T, Taketani S. Enhancement of glutathione levels in mouse
967 peritoneal macrophages by sodium arsenite, cadmium chloride and glucose/glucose oxidase.
968 Biochim Biophys Acta. 1991 Apr 17;1092(2):175–9.
969 34. Liu T, Sun L, Zhang Y, Wang Y, Zheng J. Imbalanced GSH/ROS and sequential cell
970 death. J Biochem Mol Toxicol [Internet]. 2021 Nov 2 [cited 2021 Nov 4]; Available from:
971 https://onlinelibrary.wiley.com/doi/10.1002/jbt.22942
972 35. Owen JB, Butterfield DA. Measurement of Oxidized/Reduced Glutathione Ratio. In:
973 Bross P, Gregersen N, editors. Protein Misfolding and Cellular Stress in Disease and Aging
974 [Internet]. Totowa, NJ: Humana Press; 2010 [cited 2021 Nov 4]. p. 269–77. (Methods in
975 Molecular Biology; vol. 648). Available from: http://link.springer.com/10.1007/978-1-60761-
976 756-3_18
977 36. Liu Y, Adachi M, Zhao S, Hareyama M, Koong AC, Luo D, et al. Preventing oxidative
978 stress: a new role for XBP1. Cell Death Differ. 2009 Jun;16(6):847–57.
979 37. Mayr L, Grabherr F, Schwärzler J, Reitmeier I, Sommer F, Gehmacher T, et al. Dietary
980 lipids fuel GPX4-restricted enteritis resembling Crohn's disease. Nat Commun. 2020 Apr

981 14;11(1):1775.
982 38. Forcina GC, Dixon SJ. GPX4 at the Crossroads of Lipid Homeostasis and Ferroptosis.
983 PROTEOMICS. 2019 Sep;19(18):1800311.
984 39. Benzarti M, Delbrouck C, Neises L, Kiweler N, Meiser J. Metabolic Potential of Cancer
985 Cells in Context of the Metastatic Cascade. Cells. 2020 Sep 5;9(9):2035.
986 40. Yang M, Vousden KH. Serine and one-carbon metabolism in cancer. Nat Rev Cancer.
987 2016 Oct;16(10):650–62.
988 41. Maddocks ODK, Athineos D, Cheung EC, Lee P, Zhang T, van den Broek NJF, et al.
989 Erratum: Corrigendum: Modulating the therapeutic response of tumours to dietary serine and
990 glycine starvation. Nature. 2017 Aug;548(7665):122–122.
991 42. Meiser J, Tumanov S, Maddocks O, Labuschagne CF, Athineos D, Van Den Broek N,
992 et al. Serine one-carbon catabolism with formate overflow. Sci Adv. 2016 Oct;2(10):e1601273.
993 43. Weinstabl H, Treu M, Rinnenthal J, Zahn SK, Ettmayer P, Bader G, et al. Intracellular
994 Trapping of the Selective Phosphoglycerate Dehydrogenase (PHGDH) Inhibitor **BI-4924**
995 Disrupts Serine Biosynthesis. J Med Chem. 2019 Sep 12;62(17):7976–97.
996 44. Kiweler N, Delbrouck C, Neises L, Pozdeev VI, Soriano-Baguet L, Xian F, et al.
997 Mitochondrial One-Carbon Flux has a Growth-Independent Role in Promoting Breast Cancer
998 Metastasis [Internet]. Cancer Biology; 2021 May [cited 2022 Feb 14]. Available from:
999 http://biorxiv.org/lookup/doi/10.1101/2021.05.27.445928
1000 45. Smillie CS, Biton M, Ordovas-Montanes J, Sullivan KM, Burgin G, Graham DB, et al.
1001 Intra- and Inter-cellular Rewiring of the Human Colon during Ulcerative Colitis. Cell. 2019
1002 Jul;178(3):714-730.e22.
1003 46. Le-Trilling VTK, Ebel JF, Baier F, Wohlgemuth K, Pfeifer KR, Mookhoek A, et al.
1004 Acute Cytomegalovirus Infection Modulates the Intestinal Microbiota and Targets Intestinal
1005 Epithelial Cells [Internet]. Microbiology; 2022 Mar [cited 2022 May 17]. Available from:

1006 http://biorxiv.org/lookup/doi/10.1101/2022.03.17.484735
1007 47. Rodríguez-Sánchez I, Munger J. Meal for Two: Human Cytomegalovirus-Induced
1008 Activation of Cellular Metabolism. Viruses. 2019 Mar 19;11(3):273.
1009 48. Shen L, Hu P, Zhang Y, Ji Z, Shan X, Ni L, et al. Serine metabolism antagonizes
1010 antiviral innate immunity by preventing ATP6V0d2-mediated YAP lysosomal degradation.
1011 Cell Metab. 2021 May;33(5):971-987.e6.
1012 49. Madison BB, Dunbar L, Qiao XT, Braunstein K, Braunstein E, Gumucio DL. Cis
1013 elements of the villin gene control expression in restricted domains of the vertical (crypt) and
1014 horizontal (duodenum, cecum) axes of the intestine. J Biol Chem. 2002 Sep 6;277(36):33275–
1015 83.
1016 50. Jin L, Hill KK, Filak H, Mogan J, Knowles H, Zhang B, et al. MPYS Is Required for
1017 IFN Response Factor 3 Activation and Type I IFN Production in the Response of Cultured
1018 Phagocytes to Bacterial Second Messengers Cyclic-di-AMP and Cyclic-di-GMP. J Immunol.
1019 2011 Sep 1;187(5):2595–601.
1020 51. Vidal K, Grosjean I, evillard JP, Gespach C, Kaiserlian D. Immortalization of mouse
1021 intestinal epithelial cells by the SV40-large T gene. Phenotypic and immune characterization
1022 of the MODE-K cell line. J Immunol Methods. 1993 Nov 5;166(1):63–73.
1023 52. Lee AH, Iwakoshi NN, Anderson KC, Glimcher LH. Proteasome inhibitors disrupt the
1024 unfolded protein response in myeloma cells. Proc Natl Acad Sci. 2003 Aug 19;100(17):9946–
1025 51.
1026 53. Sato T, Vries RG, Snippert HJ, Wetering M van de, Barker N, Stange DE, et al. Single
1027 Lgr5 stem cells build crypt-villus structures in vitro without a mesenchymal niche. Nature.
1028 2009 May;459(7244):262–5.
1029 54. Yin X, Farin HF, van Es JH, Clevers H, Langer R, Karp JM. Niche-independent high-
1030 purity cultures of Lgr5+ intestinal stem cells and their progeny. Nat Methods. 2014

1031 Jan;11(1):106–12.
1032 55. Sorbara MT, Ellison LK, Ramjeet M, Travassos LH, Jones NL, Girardin SE, et al. The
1033 Protein ATG16L1 Suppresses Inflammatory Cytokines Induced by the Intracellular Sensors
1034 Nod1 and Nod2 in an Autophagy-Independent Manner. Immunity. 2013 Nov 14;39(5):858–
1035 73.
1036 56. Chan B, Magalhães VG, Lemmermann NAW, Lisnić VJ, Stempel M, Bussey KA, et
1037 al. The murine cytomegalovirus M35 protein antagonizes type I IFN induction downstream of
1038 pattern recognition receptors by targeting NF-κB mediated transcription. PLOS Pathog. 2017
1039 May 25;13(5):e1006382.
1040 57. Kiweler N, Delbrouck C, Pozdeev VI, Neises L, Soriano-Baguet L, Eiden K, et al.
1041 Mitochondria preserve an autarkic one-carbon cycle to confer growth-independent cancer cell
1042 migration and metastasis [Internet]. Cancer Biology; 2021 May [cited 2022 Apr 2]. Available
1043 from: http://biorxiv.org/lookup/doi/10.1101/2021.05.27.445928
1044 58. Hiller K, Hangebrauk J, Jäger C, Spura J, Schreiber K, Schomburg D.
1045 MetaboliteDetector: comprehensive analysis tool for targeted and nontargeted GC/MS based
1046 metabolome analysis. Anal Chem. 2009 May 1;81(9):3429–39.
1047 59. Haberman Y, Karns R, Dexheimer PJ, Schirmer M, Somekh J, Jurickova I, et al.
1048 Ulcerative colitis mucosal transcriptomes reveal mitochondriopathy and personalized
1049 mechanisms underlying disease severity and treatment response. Nat Commun. 2019 Jan
1050 3;10(1):38.
1051 60. Arijs I, De Hertogh G, Lemmens B, Van Lommel L, de Bruyn M, Vanhove W, et al.
1052 Effect of vedolizumab (anti-α4β7-integrin) therapy on histological healing and mucosal gene
1053 expression in patients with UC. Gut. 2018 Jan;67(1):43–52.
1054 61. Elmentaite R, Kumasaka N, Roberts K, Fleming A, Dann E, King HW, et al. Cells of
1055 the human intestinal tract mapped across space and time. Nature. 2021 Sep 9;597(7875):250–

5.

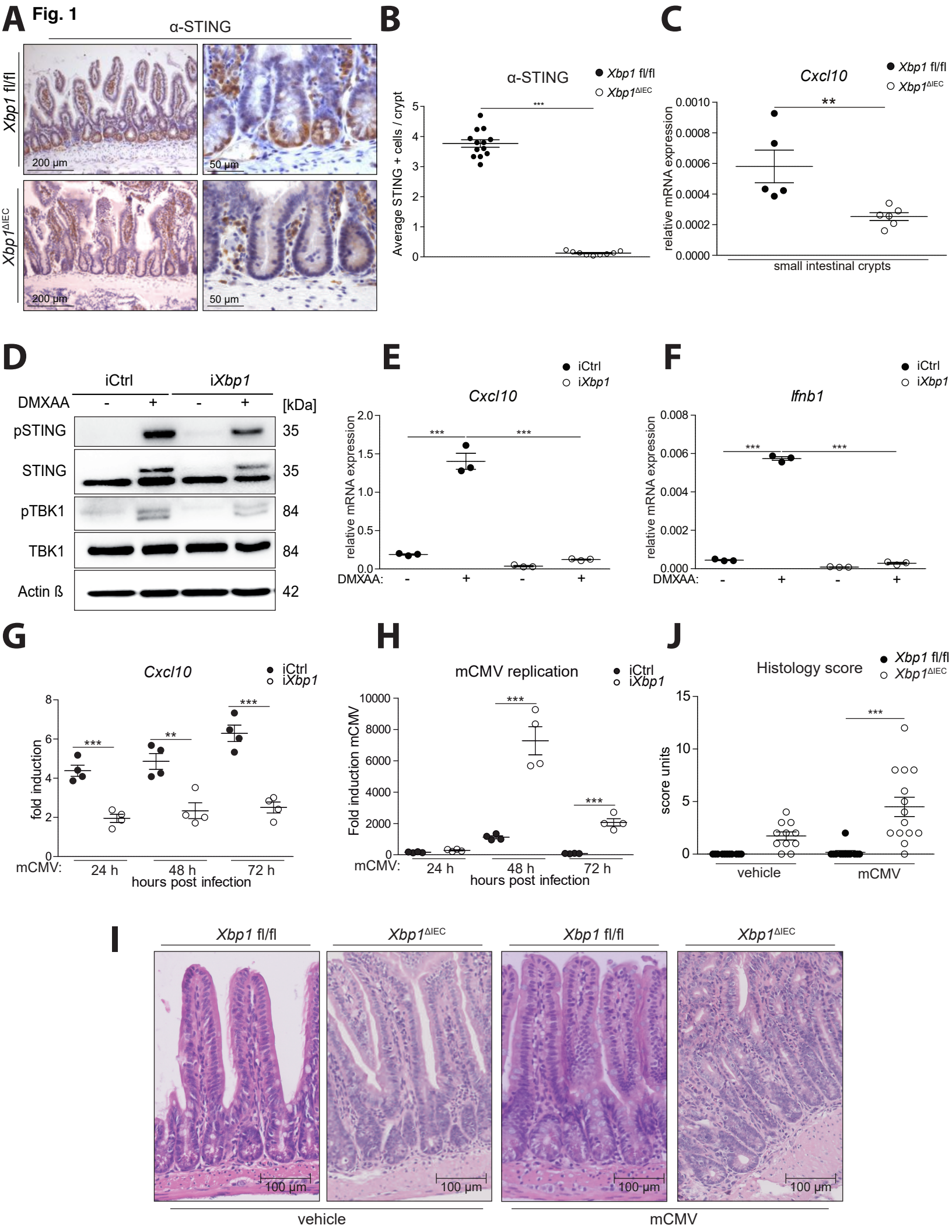
Fig. 1
A
α-STING
Xbp1 fl/fl
Xbp1ΔIEC
200 µm
50 µm
B
α-STING
Xbp1 fl/fl
Xbp1ΔIEC
Average STING + cells / crypt
***
C
Cxcl10
Xbp1 fl/fl
Xbp1ΔIEC
relative mRNA expression
**
small intestinal crypts
D
iCtrl
iXbp1
DMXAA
[kDa]
pSTING
STING
pTBK1
TBK1
Actin ß
35
35
84
84
42
E
iCtrl
iXbp1
Cxcl10
relative mRNA expression
DMXAA:
F
iCtrl
iXbp1
Ifnb1
relative mRNA expression
DMXAA:
G
Cxcl10
iCtrl
iXbp1
fold induction
mCMV:
24 h
48 h
72 h
hours post infection
H
mCMV replication
iCtrl
iXbp1
Fold induction mCMV
mCMV:
24 h
48 h
72 h
hours post infection
J
Histology score
Xbp1 fl/fl
Xbp1ΔIEC
score units
vehicle
mCMV
I
Xbp1 fl/fl
Xbp1ΔIEC
Xbp1 fl/fl
Xbp1ΔIEC
100 µm
vehicle
mCMV

Fig. S1

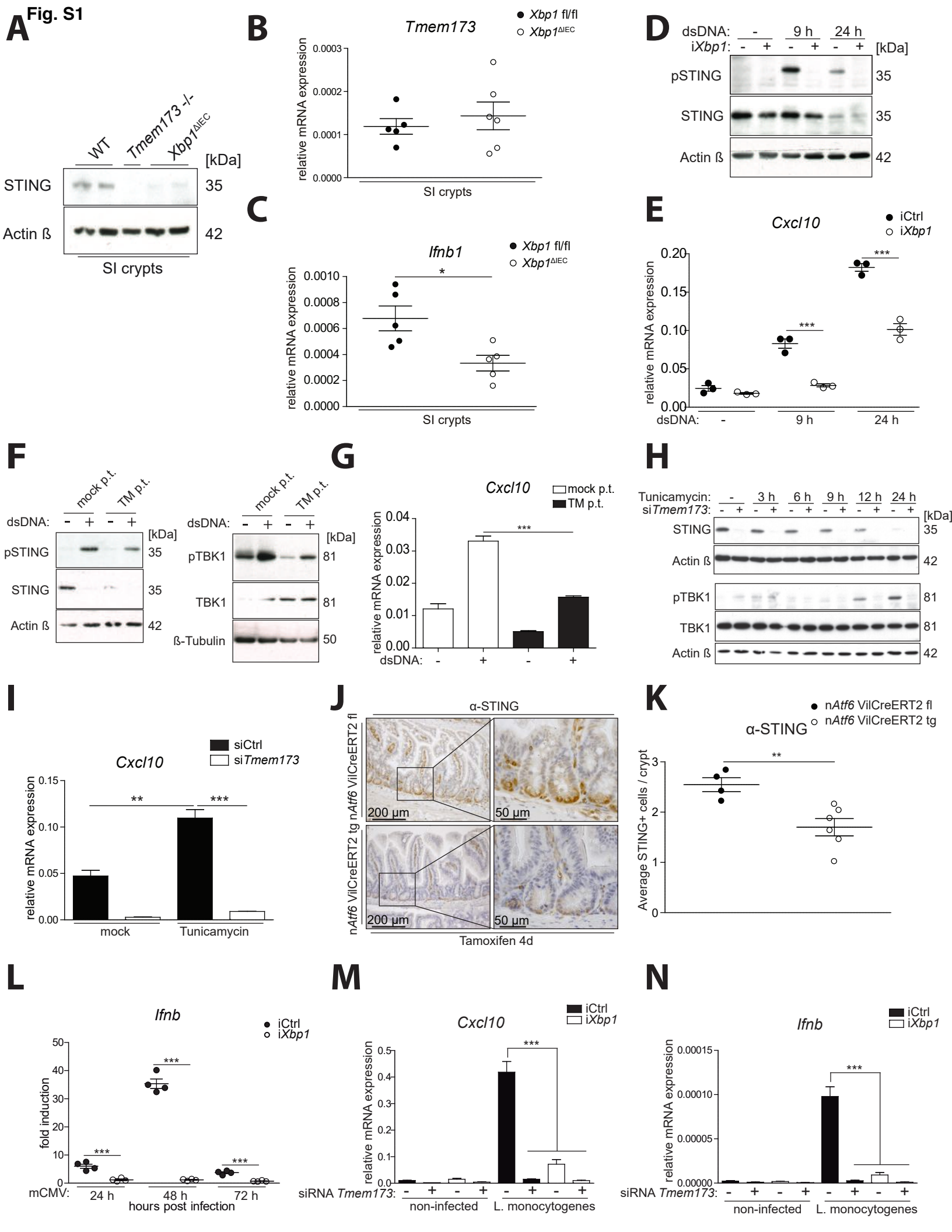
A
WT
Tmem173 -/-
Xbp1ΔIEC
[kDa]
STING
35
Actin ß
42
SI crypts
B
Tmem173
Xbp1 fl/fl
Xbp1ΔIEC
relative mRNA expression
0.0003
0.0002
0.0001
0.0000
SI crypts
C
Ifnb1
Xbp1 fl/fl
Xbp1ΔIEC
*
relative mRNA expression
0.0010
0.0008
0.0006
0.0004
0.0002
0.0000
SI crypts
D
dsDNA: - 9 h 24 h
iXbp1: - + - + - +
[kDa]
pSTING
35
STING
35
Actin ß
42
E
Cxcl10
iCtrl
iXbp1
***
***
relative mRNA expression
0.20
0.15
0.10
0.05
0.00
dsDNA: - 9 h 24 h
F
mock p.t.
TM p.t.
dsDNA: - + - +
[kDa]
pSTING
35
STING
35
Actin ß
42
mock p.t.
TM p.t.
dsDNA: - + - +
[kDa]
pTBK1
81
TBK1
81
ß-Tubulin
50
G
Cxcl10
mock p.t.
TM p.t.
***
relative mRNA expression
0.04
0.03
0.02
0.01
0.00
dsDNA: - + - +
H
Tunicamycin: - 3 h 6 h 9 h 12 h 24 h
siTmem173: - + - + - + - + - + - +
[kDa]
STING
35
Actin ß
42
pTBK1
81
TBK1
81
Actin ß
42
I
Cxcl10
siCtrl
siTmem173
**
***
relative mRNA expression
0.15
0.10
0.05
0.00
mock
Tunicamycin
J
α-STING
nAtf6 VilCreERT2 fl
nAtf6 VilCreERT2 tg
200 µm
50 µm
200 µm
50 µm
Tamoxifen 4d
K
nAtf6 VilCreERT2 fl
nAtf6 VilCreERT2 tg
α-STING
**
Average STING+ cells / crypt
3
2
1
0
L
Ifnb
iCtrl
iXbp1
***
***
***
fold induction
50
40
30
20
10
0
mCMV: 24 h 48 h 72 h
hours post infection
M
Cxcl10
iCtrl
iXbp1
***
relative mRNA expression
0.5
0.4
0.3
0.2
0.1
0.0
siRNA Tmem173: - + - + - + - +
non-infected
L. monocytogenes
N
Ifnb
iCtrl
iXbp1
***
relative mRNA expression
0.00015
0.00010
0.00005
0.00000
siRNA Tmem173: - + - + - + - +
non-infected
L. monocytogenes

Fig. 2

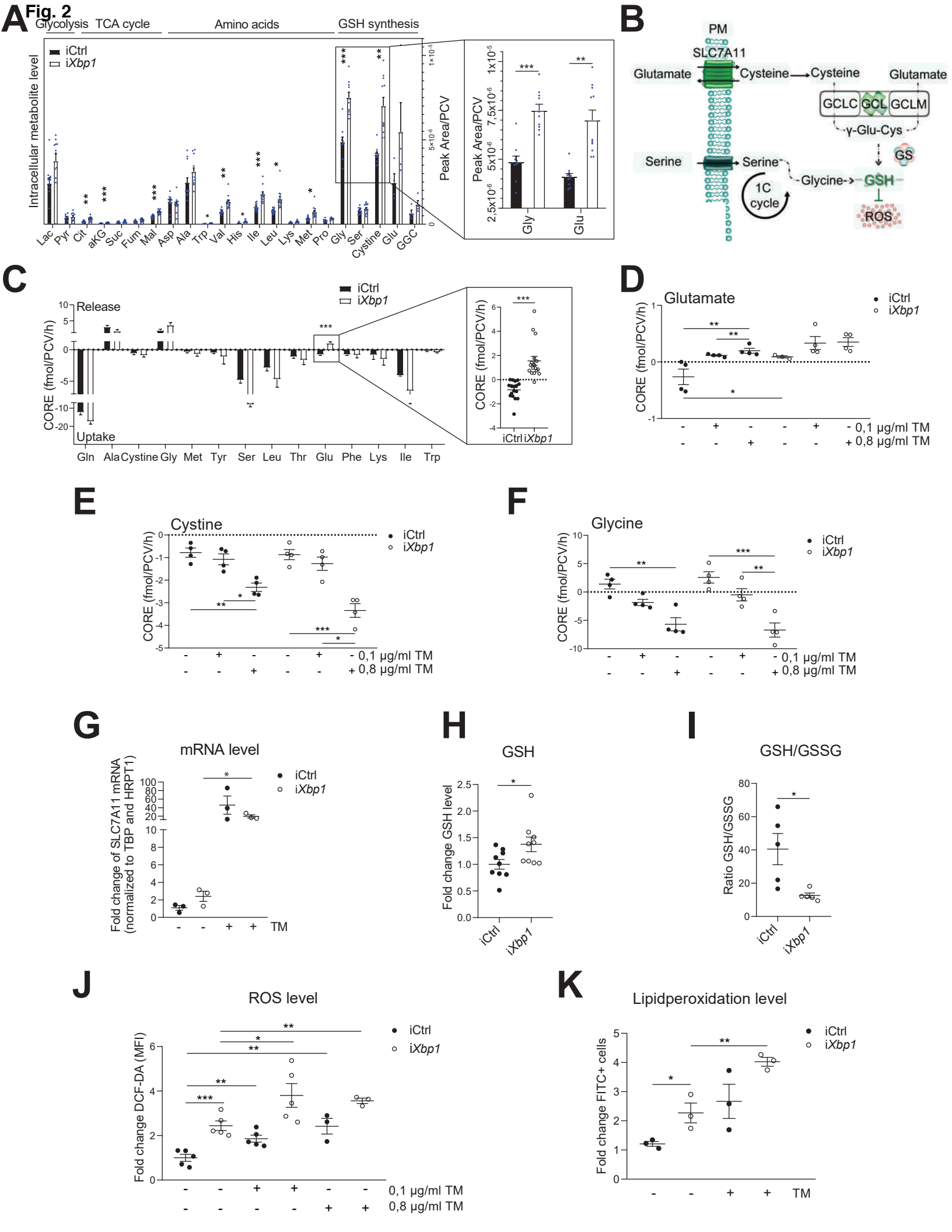
A
Glycolysis
TCA cycle
Amino acids
GSH synthesis
iCtrl
iXbp1
Intracellular metabolite level
Peak Area/PCV
Lac
Pyr
Cit
aKG
Suc
Fum
Mal
Asp
Ala
Trp
Val
His
Ile
Leu
Lys
Met
Pro
Gly
Ser
Cystine
Glu
GGC
B
PM
SLC7A11
Glutamate
Cysteine
Cysteine
Glutamate
GCLC
GCL
GCLM
γ-Glu-Cys
GS
Serine
Serine
Glycine
GSH
1C cycle
ROS
C
Release
Uptake
CORE (fmol/PCV/h)
Gln
Ala
Cystine
Gly
Met
Tyr
Ser
Leu
Thr
Glu
Phe
Lys
Ile
Trp
D
Glutamate
E
Cystine
F
Glycine
- 0,1 μg/ml TM
+ 0,8 μg/ml TM
G
mRNA level
Fold change of SLC7A11 mRNA (normalized to TBP and HRPT1)
TM
H
GSH
Fold change GSH level
I
GSH/GSSG
Ratio GSH/GSSG
J
ROS level
Fold change DCF-DA (MFI)
0,1 μg/ml TM
0,8 μg/ml TM
K
Lipidperoxidation level
Fold change FITC+ cells

Fig. S2

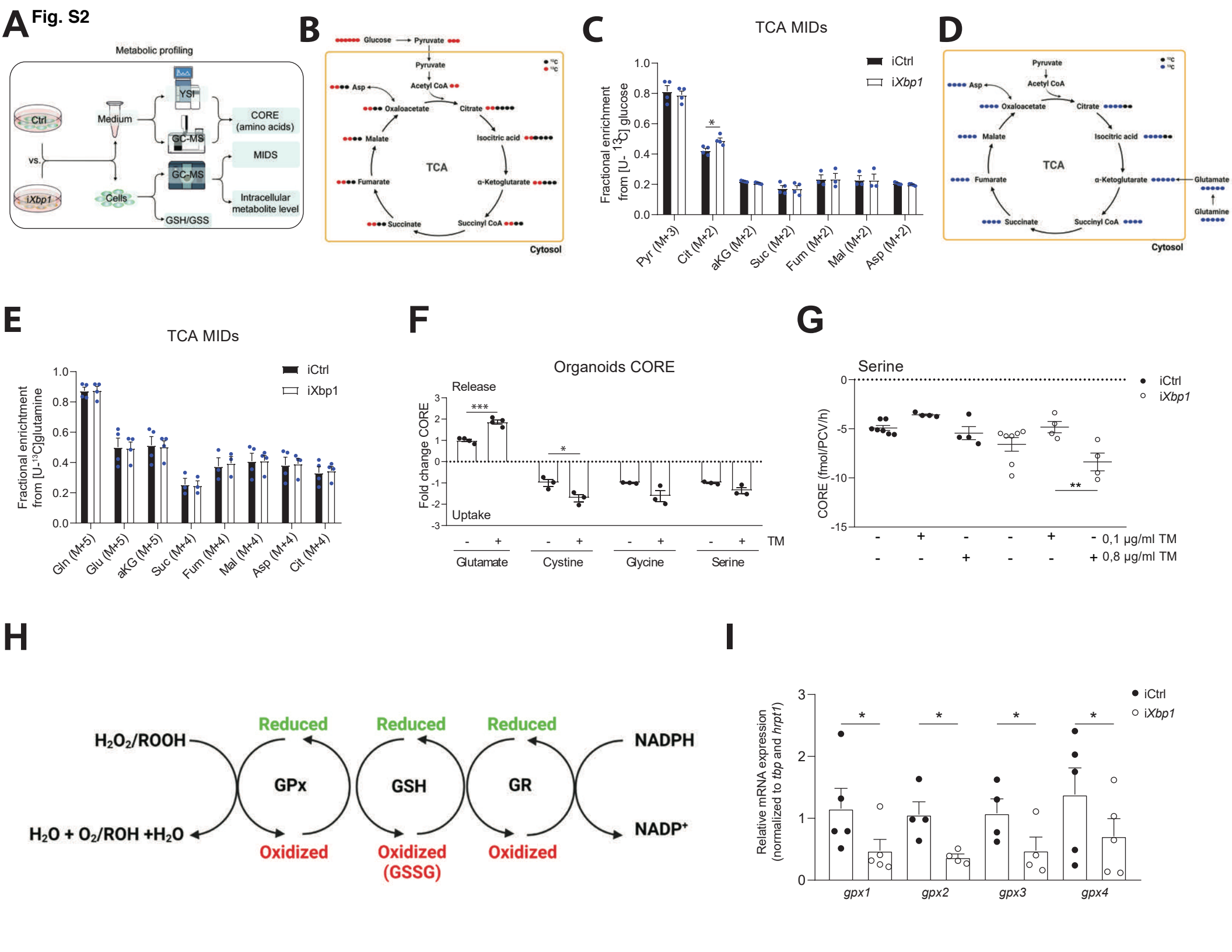
A
Metabolic profiling
Ctrl
vs.
iXbp1
Medium
Cells
YSI
GC-MS
GC-MS
GSH/GSS
CORE (amino acids)
MIDS
Intracellular metabolite level
B
Glucose
Pyruvate
Acetyl CoA
Citrate
Isocitric acid
α-Ketoglutarate
Succinyl CoA
Succinate
Fumarate
Malate
Oxaloacetate
Asp
TCA
Cytosol
C
TCA MIDs
iCtrl
iXbp1
Fractional enrichment from [U-13C] glucose
Pyr (M+3)
Cit (M+2)
aKG (M+2)
Suc (M+2)
Fum (M+2)
Mal (M+2)
Asp (M+2)
D
Glutamate
Glutamine
Cytosol
E
TCA MIDs
iCtrl
iXbp1
Fractional enrichment from [U-13C]glutamine
Gln (M+5)
Glu (M+5)
aKG (M+5)
Suc (M+4)
Fum (M+4)
Mal (M+4)
Asp (M+4)
Cit (M+4)
F
Organoids CORE
Release
Uptake
Fold change CORE
TM
Glutamate
Cystine
Glycine
Serine
G
Serine
iCtrl
iXbp1
CORE (fmol/PCV/h)
0,1 µg/ml TM
0,8 µg/ml TM
H
H2O2/ROOH
H2O + O2/ROH +H2O
Reduced
Oxidized
GPx
GSH
Oxidized (GSSG)
GR
NADPH
NADP+
I
iCtrl
iXbp1
Relative mRNA expression (normalized to tbp and hrpt1)
gpx1
gpx2
gpx3
gpx4

Fig. 3

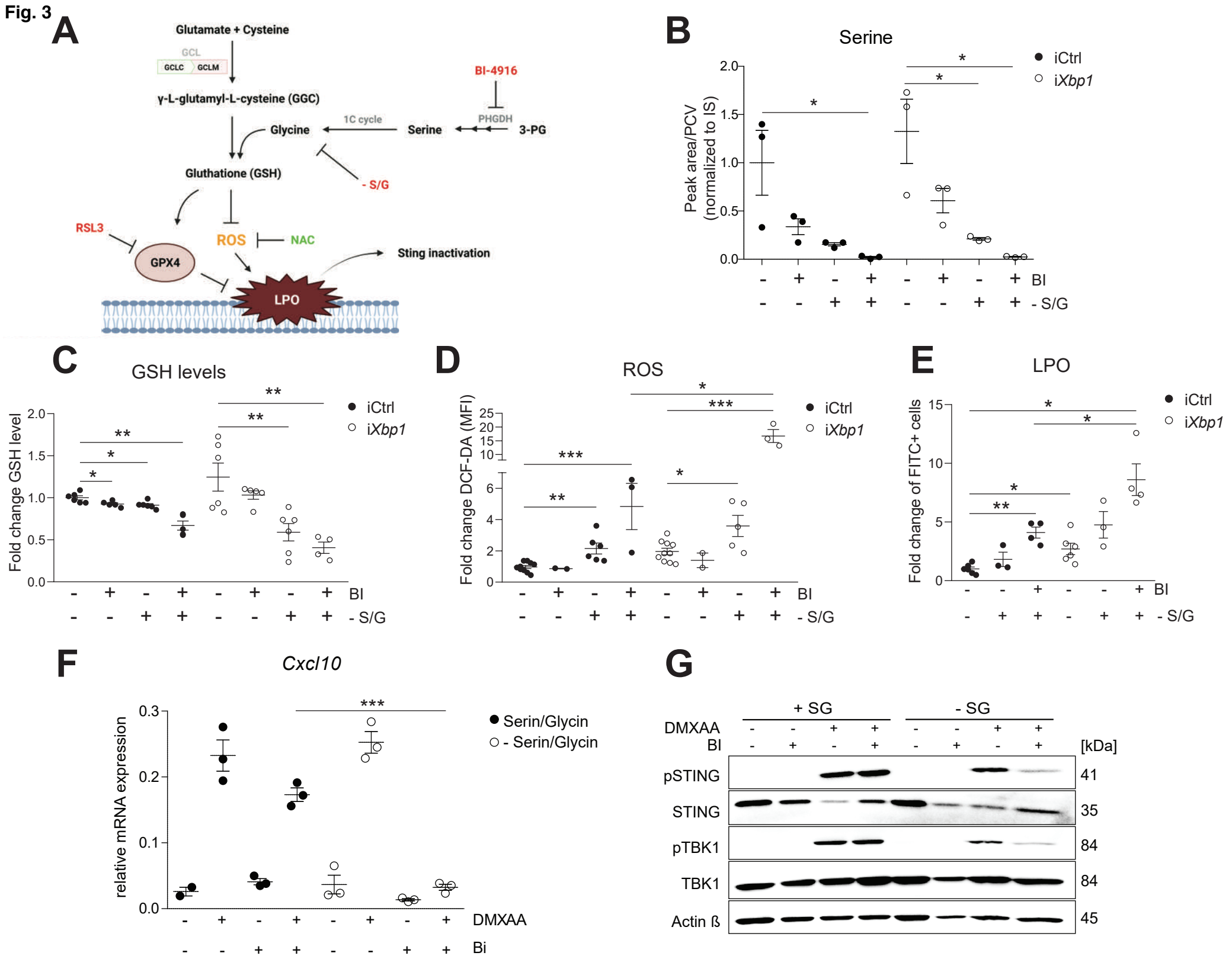
A
Glutamate + Cysteine
GCL
GCLC
GCLM
γ-L-glutamyl-L-cysteine (GGC)
Glycine
1C cycle
Serine
PHGDH
3-PG
BI-4916
Gluthatione (GSH)
- S/G
RSL3
ROS
NAC
GPX4
Sting inactivation
LPO
B
Serine
iCtrl
iXbp1
Peak area/PCV (normalized to IS)
BI
- S/G
C
GSH levels
Fold change GSH level
D
ROS
Fold change DCF-DA (MFI)
E
LPO
Fold change of FITC+ cells
F
Cxcl10
relative mRNA expression
Serin/Glycin
- Serin/Glycin
DMXAA
Bi
G
+ SG
- SG
DMXAA
BI
[kDa]
pSTING
STING
pTBK1
TBK1
Actin ß
41
35
84
84
45

Fig. S3

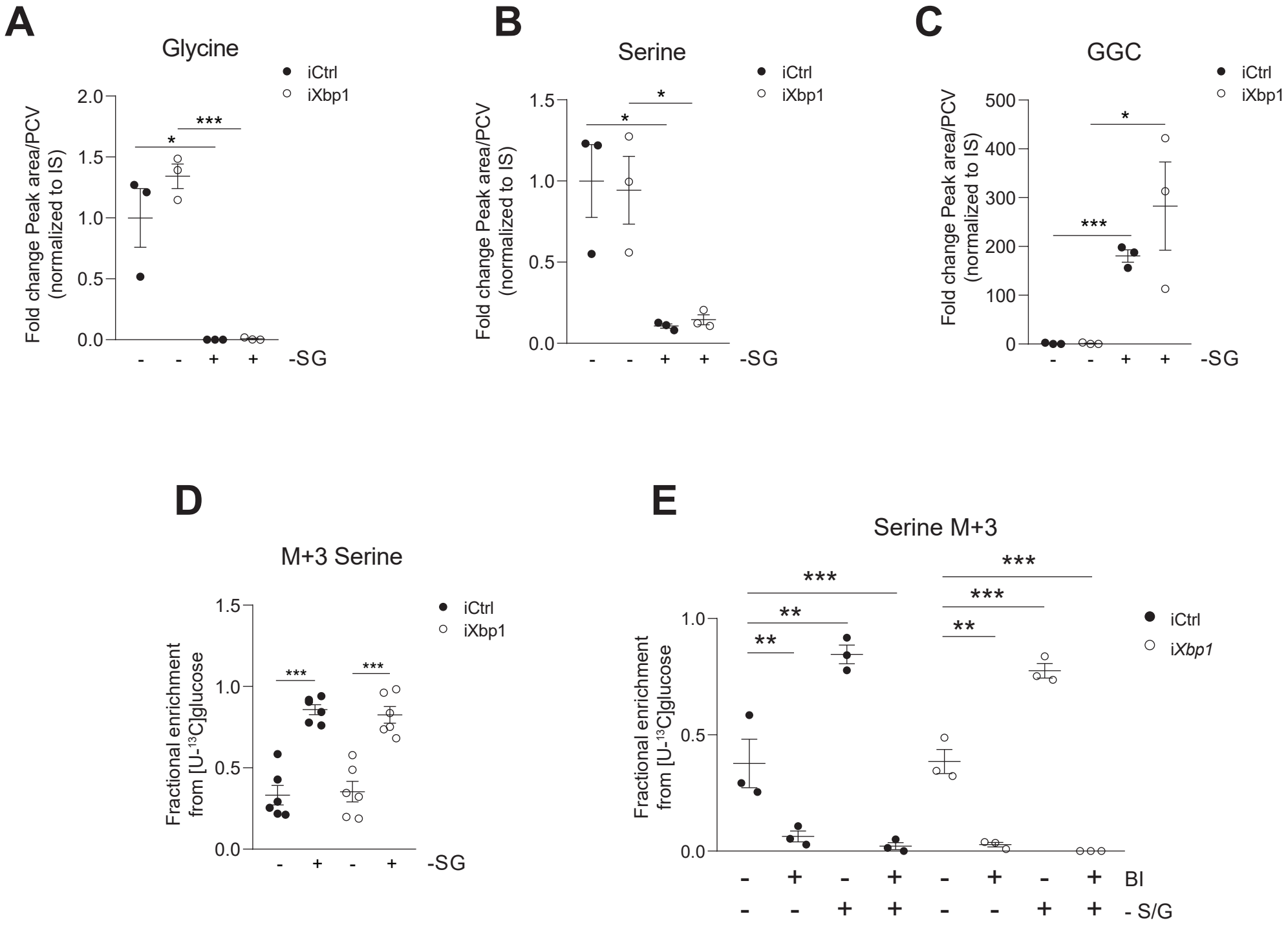
A
Glycine
iCtrl
iXbp1
Fold change Peak area/PCV (normalized to IS)
2.0
1.5
1.0
0.5
0.0
*
***
- - + + -SG
B
Serine
iCtrl
iXbp1
Fold change Peak area/PCV (normalized to IS)
1.5
1.0
0.5
0.0
*
*
- - + + -SG
C
GGC
iCtrl
iXbp1
Fold change Peak area/PCV (normalized to IS)
500
400
300
200
100
0
*
***
- - + + -SG
D
M+3 Serine
iCtrl
iXbp1
Fractional enrichment from [U-13C]glucose
1.5
1.0
0.5
0.0
***
***
- + - + -SG
E
Serine M+3
iCtrl
iXbp1
Fractional enrichment from [U-13C]glucose
1.0
0.5
0.0
***
**
**
***
***
**
- + - + - + - + BI
- - + + - - + + - S/G

Fig. S4

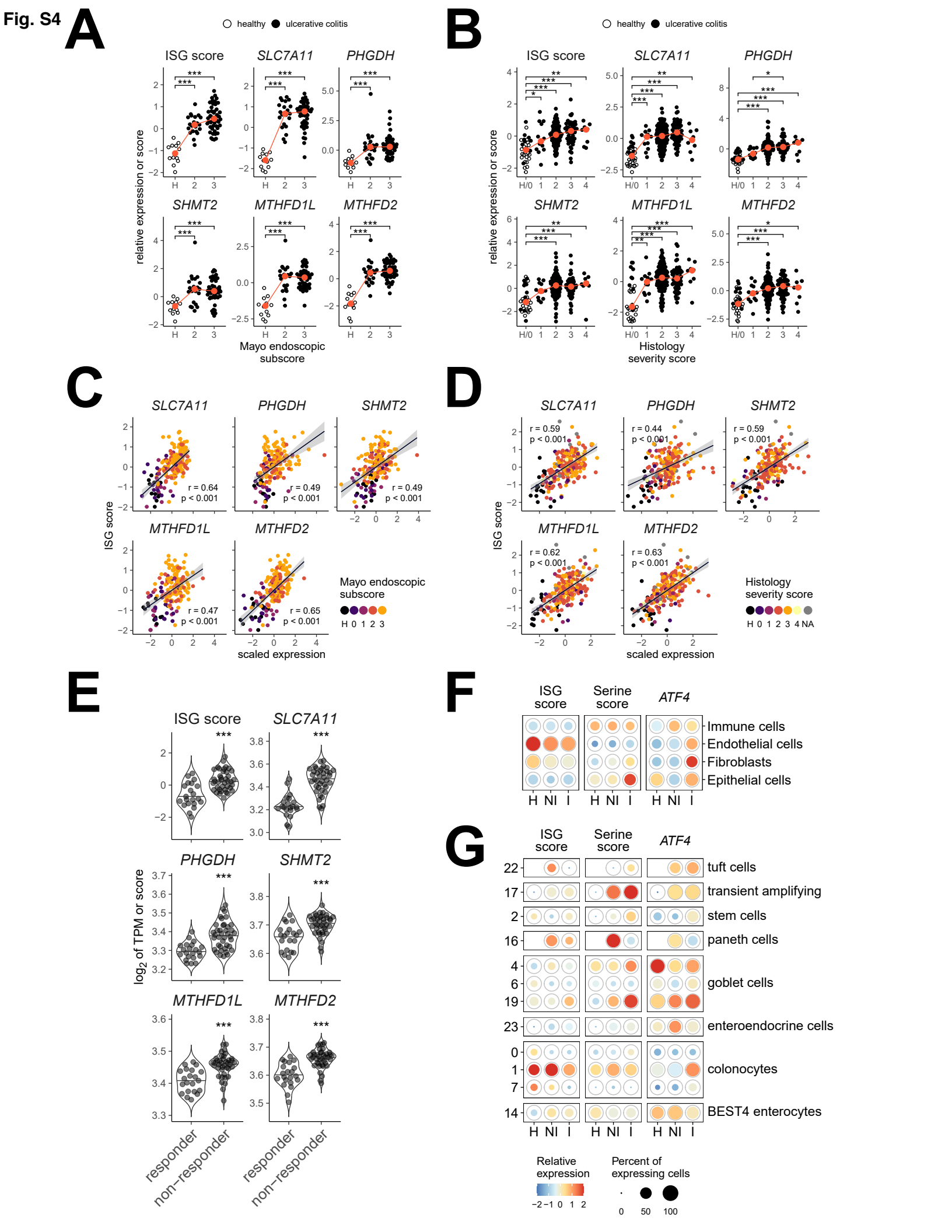
A
healthy
ulcerative colitis
ISG score
SLC7A11
PHGDH
SHMT2
MTHFD1L
MTHFD2
relative expression or score
Mayo endoscopic subscore
B
Histology severity score
C
r = 0.64
p < 0.001
r = 0.49
p < 0.001
r = 0.47
p < 0.001
r = 0.65
p < 0.001
ISG score
scaled expression
Mayo endoscopic subscore
D
r = 0.59
p < 0.001
r = 0.44
p < 0.001
r = 0.62
p < 0.001
r = 0.63
p < 0.001
Histology severity score
E
log2 of TPM or score
responder
non−responder
F
Serine score
ATF4
Immune cells
Endothelial cells
Fibroblasts
Epithelial cells
G
tuft cells
transient amplifying
stem cells
paneth cells
goblet cells
enteroendocrine cells
colonocytes
BEST4 enterocytes
Relative expression
Percent of expressing cells

Fig. 4

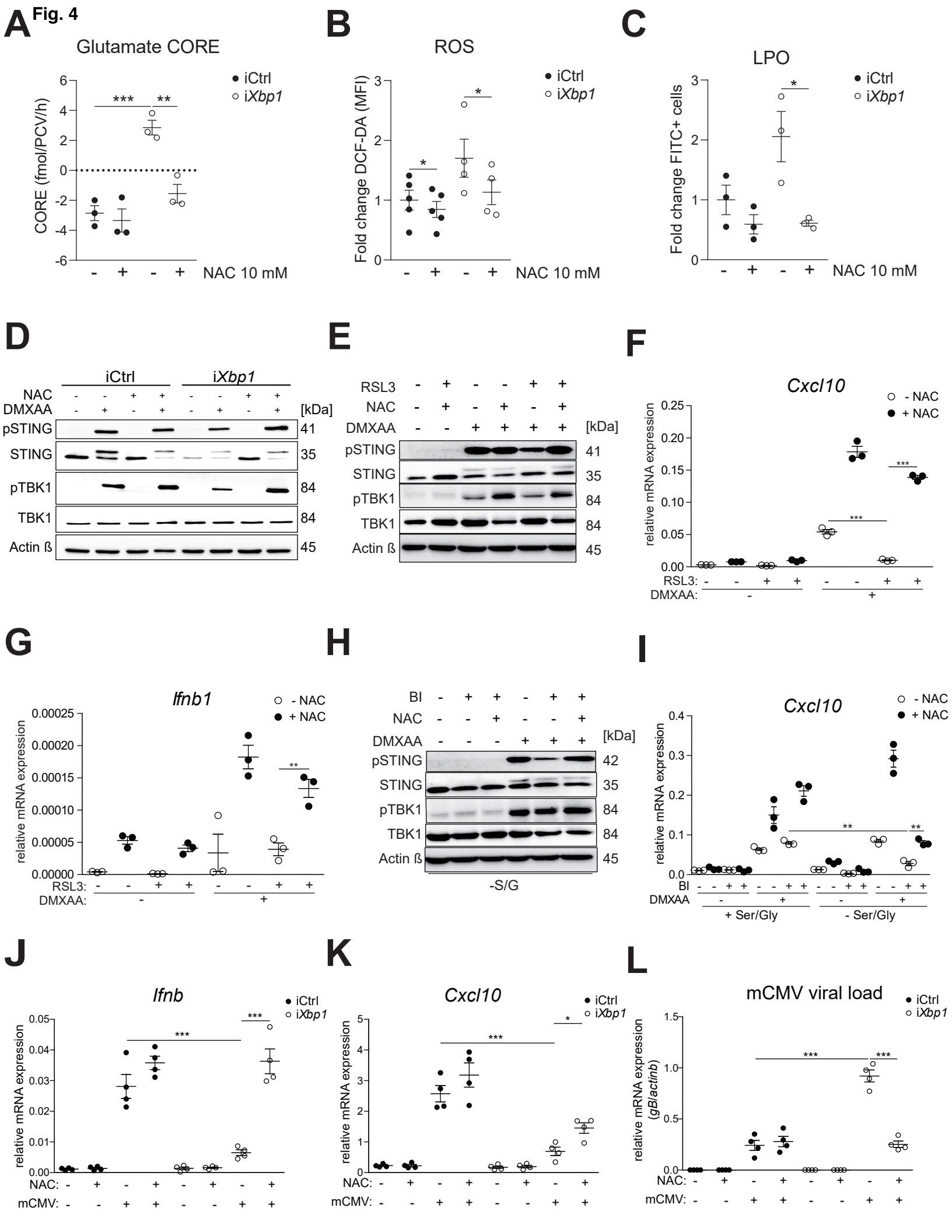
A
Glutamate CORE
CORE (fmol/PCV/h)
iCtrl
iXbp1
NAC 10 mM
B
ROS
Fold change DCF-DA (MFI)
C
LPO
Fold change FITC+ cells
D
iCtrl
iXbp1
NAC
DMXAA
[kDa]
pSTING
STING
pTBK1
TBK1
Actin ß
E
RSL3
F
Cxcl10
- NAC
+ NAC
relative mRNA expression
G
Ifnb1
H
BI
-S/G
I
+ Ser/Gly
- Ser/Gly
J
Ifnb
mCMV
K
L
mCMV viral load
(gB/actinb)

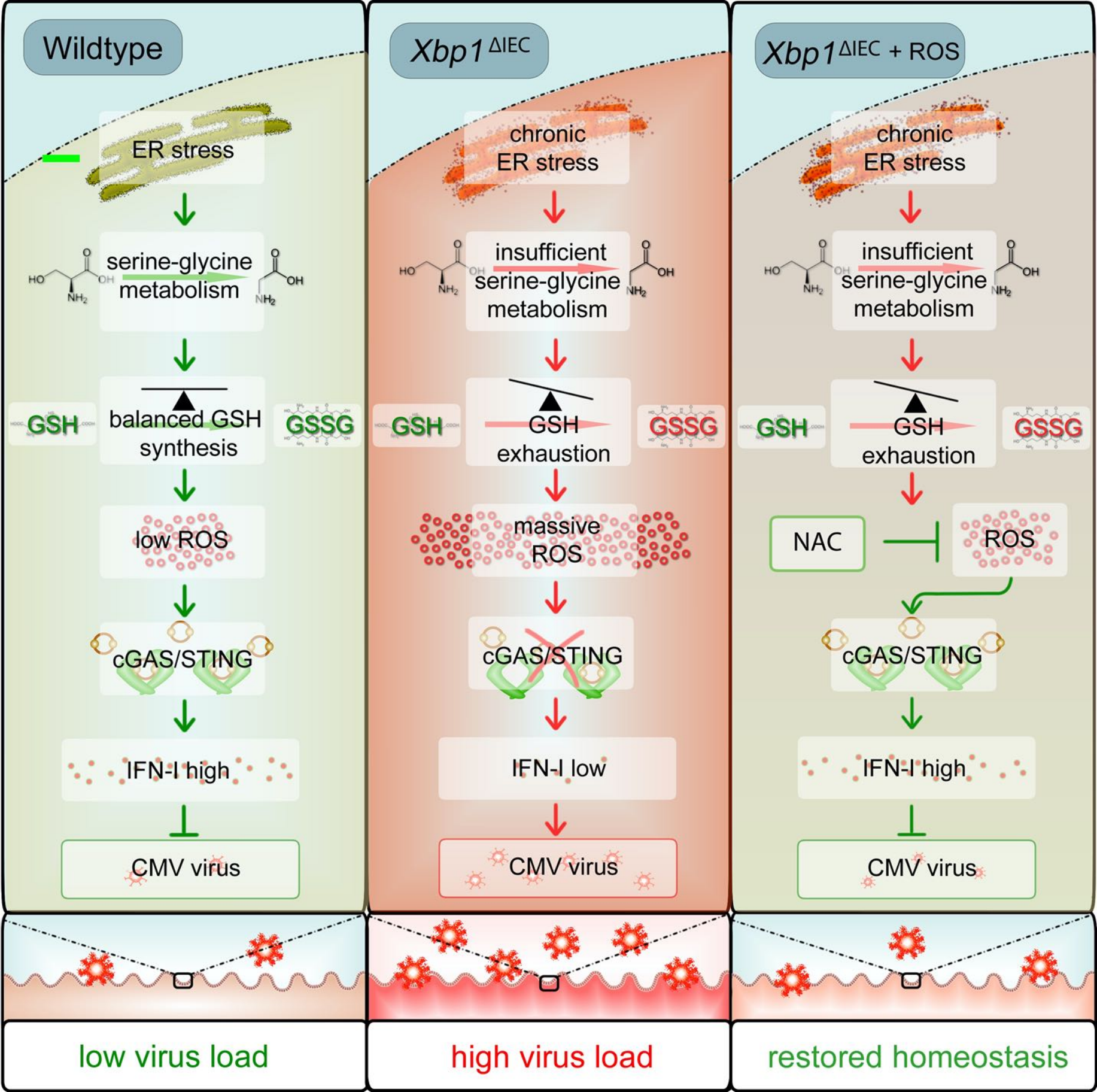
Wildtype
ER stress
serine-glycine metabolism
GSH
balanced GSH synthesis
GSSG
low ROS
cGAS/STING
IFN-I high
CMV virus
Xbp1 ΔIEC
chronic ER stress
insufficient serine-glycine metabolism
GSH
GSH exhaustion
GSSG
massive ROS
cGAS/STING
IFN-I low
CMV virus
Xbp1 ΔIEC + ROS
chronic ER stress
insufficient serine-glycine metabolism
GSH
GSH exhaustion
GSSG
NAC
ROS
cGAS/STING
IFN-I high
CMV virus
low virus load
high virus load
restored homeostasis